

Evaluation of ozone trends in the mesosphere/lower thermosphere using a new merged dataset of ozone profiles

Monika E. Szlag¹, Viktoria F. Sofieva¹, Edward Malina², Pekka T. Verronen^{1,3}, Michelle L. Santee⁴, Manuel López-Puertas⁵, Bernd Funke⁵, Gabriele Stiller⁶, Alexandra Laeng⁶, Kaley A. Walker⁷, Patrick E. Sheese⁷, Mark E. Hervig⁸, Benjamin T. Marshall⁹

¹ Finnish Meteorological Institute, Helsinki, Finland

² ESA/ESRIN, Frascati, Italy

³ Sodankylä Geophysical Observatory, University of Oulu, Sodankylä, Finland

⁴ Jet Propulsion Laboratory, California Institute of Technology, Pasadena, California, USA

⁵ Instituto de Astrofísica de Andalucía, CSIC, Granada, Spain

⁶ Karlsruhe Institute of Technology, Karlsruhe, Germany

⁷ Department of Physics, University of Toronto, Toronto, Canada

⁸ GATS, Driggs, Idaho, USA

⁹ GATS, Hampton, Virginia, USA

Correspondence to: monika.szlag@fmi.fi

Abstract. In recent years, the need for high-quality long-term mesospheric ozone records has become increasingly evident, as they are essential for understanding chemical, dynamical, and radiative processes in the middle and upper atmosphere and their coupling with the lower layers. Here, we present a new merged dataset of ozone profiles in the middle atmosphere (METEOR-O₃), created from several limb-viewing satellite instruments: HALOE, GOMOS, MIPAS, ACE-FTS, MLS, and SOFIE. The merged dataset covers the period from 1991 to 2023 and provides deseasonalized ozone anomalies in 10° latitude bins between 80°S and 80°N, from approximately 22 km to 100 km. The deseasonalized ozone anomalies are used for global and seasonal trend analysis. The results show positive upper stratospheric ozone trends in both hemispheres, with magnitudes of 1–2% per decade between 35 and 45 km, indicating continued ozone recovery consistent with previous assessments. In contrast, mesospheric ozone (above ~60 km) exhibits negative trends of -1 to -3% per decade, with the strongest decreases of about -8 to -12% per decade between 80 and 90 km. Seasonal analyses confirm positive trends in the upper stratosphere across all seasons and persistent negative trends in the upper mesosphere, strongest at high latitudes above 80 km. The METEOR-O₃ dataset provides the first global, long-term merged record suitable for detailed studies of mesospheric/lower thermospheric ozone variability and trend evaluation, providing valuable information for model validation and assessments of upper atmospheric changes.

32 1 Introduction

33 Understanding long-term trends in the mesosphere and lower thermosphere (MLT, ~50-120 km) is becoming increasingly
34 important as they can serve as a valuable indicator of climatic change. Trends in the MLT region exhibit significant variability,
35 which can be influenced by solar activity, atmospheric dynamics, and anthropogenic factors (Laštovička, 2017; 2023; and
36 references therein). Over the last few years, the upper atmosphere has been widely studied, particularly concerning long-term
37 trends. While temperature remains the most extensively studied, other parameters (winds, water vapour, minor constituents)
38 have been analysed as well (Laštovička, 2023, Cnossen et al., 2024; and reference therein).

39 The middle and upper atmosphere is experiencing a global mean negative temperature trend observed across datasets and
40 models caused by the increasing concentration of CO₂ (Laštovička, 2006a; Qian et al., 2021; Cnossen, 2020). Increases in CH₄
41 and H₂O, along with decreasing stratospheric O₃, contribute to cooling in the stratosphere and mesosphere, but their influence
42 becomes negligible in the upper thermosphere (Cnossen et al., 2024 and references therein). The mesospheric cooling trend
43 has been observed in ground-based and satellite measurements with a magnitude of about 0.5-2 K per decade (Yuan et al.,
44 2019; Bailey et al., 2021; Das, 2021; Li et al., 2021). Numerical simulations generally confirm the cooling trend except for the
45 summer upper mesosphere, which shows near-zero or slightly positive temperature trends, likely reflecting dynamical effects
46 (Qian et al., 2019; Solomon et al., 2019).

47 The long-term trends in dynamical processes, which are important in the MLT, are more complex. Observations and
48 simulations reveal large spatial and temporal variability in wind trends, often differing between regions and seasons (Qian et
49 al., 2019; Wilhelm et al., 2019). Research on atmospheric waves has been limited and concentrating mainly on tides
50 (Laštovička, 2023). No significant long-term changes in diurnal tides have been observed, while semidiurnal components show
51 mixed results that vary with altitude and latitude (Wilhelm et al., 2019). Overall, dynamical trends in the MLT are poorly
52 constrained and regionally dependent, remaining a major source of uncertainty in understanding the MLT's long-term
53 evolution (Laštovička, 2023 and references therein).

54 Mesospheric ozone plays an important role in atmospheric chemistry, dynamics, and energy balance, yet it remains one
55 of the least-investigated parameters (Laštovička, 2023). Variations in its concentration can substantially influence the
56 composition and behavior of the upper and middle atmosphere, thereby affecting the coupling between different atmospheric
57 layers (Sinnhuber et al., 2012; Seppälä et al., 2009, 2024). In recent years, there has been a growing scientific interest in
58 understanding solar-driven changes in ozone and temperature in the mesosphere and upper stratosphere (Salminen et al., 2019;
59 Szelag et al., 2022; Seppälä et al. 2024). These variations, although occurring alongside the rapid climate change driven by
60 anthropogenic greenhouse gas emissions, have the potential to regulate regional climate on annual to decadal timescales
61 (Baumgaertner et al., 2011; Langematz et al., 2005; Maliniemi et al., 2014; Rozanov et al., 2005, 2012; Seppälä et al., 2009,
62 2013). Understanding these complex interactions between human-induced and naturally driven climate variability is
63 particularly important in the polar regions, which are experiencing some of the most significant changes.

64 While individual satellite instruments provide ozone measurements in the mesosphere, their operation is limited in time.
65 To date, a comprehensive merged data set combining multiple sources of mesospheric ozone data is not available, and an
66 assessment of global mesospheric ozone trends has not been conducted. Previous analyses (Bizuneh et al., 2022; Huang et al.,
67 2014; Nath and Sridharan, 2014) based on 10-15 years of SABER (Sounding of the Atmosphere using Broadband Emission
68 Radiometry) data were confined to narrow latitude ranges (5°N - 15°N) or limited to lower and middle latitudes (48°S - 48°N),
69 thereby restricting insight into global long-term mesospheric ozone variability. Moreover, SABER ozone data are known to
70 suffer from quality limitations (Mlynczak, private communication; López-Puertas et al., 2023), underscoring the need for
71 improved observational datasets and longer time series to establish reliable long-term trends.

72 In this paper, we introduce a new merged dataset of ozone profiles in the middle atmosphere, created using the data from
73 several limb and occultation instruments: HALOE (Halogen Occultation Experiment), GOMOS (Global Ozone Monitoring by
74 Occultation of Stars), MIPAS (Michelson Interferometer for Passive Atmospheric Sounding), ACE-FTS (Atmospheric
75 Chemistry Experiment - Fourier Transform Spectrometer), MLS (Microwave Limb Sounder), and SOFIE (Solar Occultation
76 For Ice Experiment). The paper is organized as follows. In Section 2, we provide short descriptions of the data used for the
77 merged dataset. In Section 3, we describe the data preparation for the merging procedure, which is discussed in Section 4.
78 Section 5 describes the new merged METEOR- O_3 dataset. Section 6 is dedicated to trends analyses in the upper atmosphere.
79 The summary (Section 7) concludes the paper.

80 **2 Data**

81 For the merged dataset of ozone mixing ratio profiles, we used profiles from the limb and occultation instruments that
82 provide ozone data in the mesosphere and the lower thermosphere: HALOE, GOMOS, MIPAS, ACE-FTS, MLS, and SOFIE,
83 as described below. For several instruments, the data are from the HARMonized dataset of Ozone profiles (HARMOZ)
84 collection (Sofieva et al., 2013).

85 **2.1 HALOE**

86 The Halogen Occultation Experiment (HALOE) was a solar occultation instrument that operated on board the Upper
87 Atmosphere Research Satellite (UARS) from September 1991 until November 2005 (Russell et al., 1993). HALOE typically
88 recorded about 15 sunrise and sunset events per day, between 3 km and 130 km altitude, with a vertical resolution of about 2
89 km. HALOE was able to cover the entire latitude range from 80°S to 80°N within a time span of about two to six weeks,
90 depending on the time of year.

91 Here we use Level 2 data obtained with the version 19 processing algorithm. Ozone observations were performed using
92 a broadband spectral channel centered around $9.6\ \mu\text{m}$. The error estimates account for random noise and altitude-dependent

93 quasi-systematic uncertainties, primarily arising from aerosol correction inaccuracies. These errors are about 5-10% in the
94 middle and upper atmosphere, increasing to around 30% near the 100 hPa level (Bhatt et al., 1999).

95 **2.2 GOMOS**

96 The Global Ozone Monitoring by Occultation of Stars (GOMOS) was a stellar occultation instrument that operated on
97 board Envisat (ENVironmental SATellite) over 2002-2012 (Bertaux et al., 2010; Kyrölä et al., 2010). Ozone profiles are
98 retrieved from the ultraviolet (UV) and visible spectrometer measurements at wavelengths between 250 and 692 nm. The main
99 dataset consists of nighttime ozone profiles with solar zenith angle larger than 105° (equatorial crossings at 10 p.m local time),
100 which are retrieved from atmospheric transmittance spectra. For this study, we use GOMOS ozone profiles obtained with the
101 ALGOM2s v1.0 processor (Sofieva et al., 2017a). ALGOM2s is identical to the ESA IPF v6 processor in the stratosphere and
102 MLT but has improved data quality in the upper troposphere/lower stratosphere (UTLS).

103 GOMOS provides stratospheric and MLT ozone profiles with a vertical resolution of 2 km below 30 km, 3 km above
104 30 km, with a linear transition between (Tamminen et al., 2010). The vertical resolution of the GOMOS ozone profiles is the
105 same for all occultations due to the Tikhonov-type target-resolution regularization (Kyrölä et al., 2010; Sofieva et al., 2004).
106 The stellar flux recorded by GOMOS, and thus signal-to-noise ratio and precision of retrieved profiles, depends on stellar
107 magnitude and spectral class. The estimated random uncertainty of GOMOS ozone profiles in the MLT is 1-7 % (Tamminen
108 et al., 2010).

109 GOMOS exploits a self-calibrating measurement principle, therefore high stability of the GOMOS data is expected
110 (Kyrölä et al., 2010). It turned out that it is important to exclude the ozone data from the stars with insufficient UV-flux. In
111 our study, we used the GOMOS data from the HARMOZ dataset, which consists of valid data only.

112 **2.3 MIPAS**

113 The Michelson Interferometer for Passive Atmospheric Sounding (MIPAS) was an infrared limb emission spectrometer
114 that was flown on the Envisat platform (Fischer et al., 2008). In 2002-2004, the instrument operated at full spectral resolution.
115 Due to a failure of the instrument's mirror slide in 2004, operations were suspended for almost 9 months and were resumed in
116 January 2005 with reduced spectral but improved vertical resolution. These operations continued until the loss of
117 communications with the ENVISAT platform in April 2012. Most of the time MIPAS observed the 6–68 km altitude range in
118 its nominal mode (hereafter referred to as MIPAS_NOM). After 2005, it also pointed to higher altitudes less frequently (about
119 one out of five days) in its middle atmosphere (MA, 20-102 km) and upper atmosphere (UA, 40-102 km) measurement modes
120 (hereafter collectively referred to as MIPAS_MA_UA). The equator crossings occurred at approximately 10 am and 10 pm
121 local time.

122 Stratospheric ozone profiles are retrieved from MIPAS/ENVISAT limb emission spectra. In this work, we use version
123 V8R_O3_261/561/661 ozone data derived with the scientific MIPAS level 2 processor developed by Karlsruhe Institute of

124 Technology and Instituto de Astrofísica de Andalucía (IMK/IAA). The retrieval is performed via constrained inverse modelling
125 of limb radiances. A detailed description can be found in von Clarmann et al. (2003, 2009). The data version used in this work
126 is retrieved from new Level 1 spectra (version V8). Improvements in the Level 2 retrieval strategy are described in Kiefer et
127 al. (2023), and López-Puertas et al. (2023) for the NOM and MA/UA modes, respectively.

128 Due to their different data characteristics, the two MIPAS measurement periods are usually treated as two independent datasets.
129 Their processing schemes are different, and the vertical resolution of the early MIPAS period is lower than that of the later
130 period: 5 - 8 km vs. 4 - 6 km for retrieved ozone in the mesosphere from MIPAS_NOM measurements. Therefore, and because
131 of their short temporal coverage, data of the first measurement period (2002-2004) have not been considered in this study.
132 The total random error in the mesosphere from MIPAS_NOM observations is on the order of 8% (at 50 km) to 30% (at 70
133 km), with a total systematic error in the same range. For MIPAS_MA_UA observations, the total random error ranges from
134 3% at 50 km altitude to 20%–30% in the upper mesosphere/lower thermosphere, being larger in daytime than in nighttime.
135 The total systematic error is rather constant over all altitudes and is in the range of 7 to 10%, including non-LTE (non-Local
136 Thermodynamic Equilibrium) errors from uncertainties in the collisional and kinetic rate constants and the abundances of
137 atmospheric species required for the non-LTE modelling (Kiefer et al., 2023; López-Puertas et al., 2023).

138 **2.4 ACE-FTS**

139 The Atmospheric Chemistry Experiment - Fourier Transform Spectrometer (ACE-FTS) on board the Canadian Science
140 Satellite (SciSat) satellite (Bernath, 2017; Bernath et al., 2005) has been providing the data since February 2004 to present. It
141 measures from about 85°N to 85°S with complete coverage every 3 months. The ACE-FTS is a high-spectral-resolution (0.02
142 cm⁻¹) Fourier transform spectrometer observing the 2.2-13 μm range (Bernath et al., 2005). Using solar occultation, it provides
143 vertical profiles for over 30 atmospheric species.

144 For each occultation, the ACE-FTS retrieval algorithm determines volume mixing ratio profiles by applying a global
145 non-linear least-squares fitting technique, matching observed spectra with those produced by a forward model. A full
146 description of this retrieval processor can be found in Boone et al. (2005). The current version of the ACE-FTS data set used
147 for HARMOZ is v5.2, as described in (Boone et al., 2023). For ozone, the retrieval uses 40 microwindows between 829 and
148 2673 cm⁻¹ and accounts for 15 different interfering species and subsidiary isotopologues. The altitude range of the retrieved
149 ozone profiles is about 5-95 km, with a vertical resolution of approximately 3-4 km.

150 The ACE-FTS dataset includes quality flags (Sheese et al., 2015). For HARMOZ, data points with flag values > 0 at a
151 given altitude and any profiles with flags 4–6 were removed. A recent validation study (Sheese et al., 2022) found that v4.1
152 ACE-FTS ozone (the latest version for which validation has been performed) exhibits a bias relative to other instruments of
153 approximately -1% to +5% in the lower stratosphere, +2 to +9% in the middle stratosphere, and up to about +15% in the upper
154 stratosphere. The estimated precision of v4.1 ozone is ~6–10% between 20 and 45 km and ~5–10% above 45 km.

156 The Microwave Limb Sounder (MLS), launched as part of NASA's Aura mission in July 2004, measures millimeter-
157 and submillimeter-wavelength thermal emission from the limb of Earth's atmosphere (Waters et al., 2006). The Aura MLS
158 field of view points in the direction of orbital motion and vertically scans the limb in the orbit plane, providing approximately
159 3500 daily vertical profiles of 16 trace gases, temperature, geopotential height, relative humidity with respect to ice, and cloud
160 ice water content and path spaced at ~165 km along the orbit track from 82°S to 82°N latitude on every orbit. Aura is in a sun-
161 synchronous orbit with a 1:45 p.m. local time ascending equator-crossing time; thus, MLS samples a given latitude on either
162 the ascending (mainly day) or descending (mainly night) portions of each orbit at the same local solar time.

163 Here we use version 5 Level 2 MLS ozone measurements. The MLS retrieval algorithms, which employ an optimal
164 estimation approach, are "tomographic" in nature, exploiting information from multiple consecutive limb scans to
165 simultaneously estimate the two-dimensional (along-track and vertical) state of the atmosphere over multiple Level 2 profiles
166 (Livesey et al., 2006). The quality and resolution of the version 5 MLS data vary by product and with altitude. For ozone, the
167 vertical resolution ranges from ~2.5–3 km in most of the stratosphere to 7 km at 0.001 hPa (Livesey et al., 2022). The single-
168 profile precision degrades from 0.04 ppmv at 100 hPa to 0.1 ppmv at 10 hPa, 0.2 ppmv at 1 hPa, 1.1 ppmv at 0.01 hPa, and
169 3.4 ppmv at 0.001 hPa. However, precision is generally improved by averaging (with the precision of an average of N profiles
170 being a factor of the square root of N times smaller than the precision of an individual profile). The systematic uncertainty of
171 version 5 ozone data is in the range 0.1 to 0.3 ppmv (on average 7-25%) over most of the stratosphere and mesosphere but
172 increases to 0.9 ppmv (~30%) at 0.001 hPa (~95 km).

173 **2.6 SOFIE**

174 The Solar Occultation For Ice Experiment (SOFIE) operated on board NASA's Aeronomy of Ice in the Mesosphere
175 (AIM) satellite from April 2007 until March 2023 (Russell et al., 2009). It conducted measurements across 16 spectral bands,
176 covering wavelengths from 0.29 to 5.32 micrometers, and provided vertical profiles of temperature and key atmospheric
177 constituents, including H₂O, O₃, CO₂, CH₄, and NO (Hervig et al., 2009a, 2009b; Marshall et al., 2011). The instrument covered
178 high latitudes of about 65°–85° in both hemispheres with a vertical resolution of about 1.6 km. SOFIE measured 15 sunrise
179 and sunset events per day between about 20 km and 105 km (Das et al., 2023; Gordley et al., 2009a, b).

180 Here we use ozone data from SOFIE Level 2 processing (v1.3) (Gordley et al., 2009b). Ozone measurements are made
181 using two broadband filters at 292 nm (roughly 50-105 km) and 330 nm (from the tropopause to 60 km), with the former
182 located in a spectral region of strong absorption that offers increased sensitivity in the mesosphere. These profiles are then
183 combined to form a continuous ozone dataset extending from approximately the tropopause to 105 km. Refraction and
184 Rayleigh scattering are accounted for in the SOFIE forward model. Additional interference comes from stratospheric aerosols
185 below ~35 km (currently not corrected) and polar mesospheric clouds near 80–90 km during polar summer (corrected using

186 the 330 nm band). Ozone errors result from uncertainties in the observations or the forward model. The combined random and
 187 systematic uncertainty in the O₃ mixing ratio is 3.4-6.5% over the altitude range 30-100 km (Das et al., 2023).

188

189 2.7 METEOR-O₃ Data Summary

190 Information on the individual datasets specifically included in METEOR-O₃ is summarized in Table 1. All datasets used
 191 to create the merged dataset have a vertical resolution of approximately 2-7 km in the MLT. Ozone measurements from the
 192 various satellite instruments provide global coverage and were obtained at different local times. The time series of the number
 193 of available ozone profiles per month from each dataset is shown in Figure 1. Note that for some datasets, the selected period
 194 is shorter than their full operational period; for example, MIPAS_NOM data are included starting from 2005, as in Sofieva et
 195 al. (2017, 2023). For instruments measuring in different illumination conditions (for example, daytime and nighttime
 196 measurements by MLS and MIPAS_NOM), the number of profiles per month is nearly identical. Latitudinal coverage of some
 197 of the datasets is illustrated in the Supplement (Figures S1 and S2). The best spatial coverage is provided by instruments with
 198 dense sampling (MLS and MIPAS_NOM), while solar occultation instruments contribute 14-15 sunrise and sunset
 199 measurements per day. SOFIE data are limited to the polar regions, and its sampling pattern changes around 2016 due to shifts
 200 in sunrise/sunset measurement geometry (Fig. S1). Consequently, for Southern Hemisphere high latitudes the SOFIE anomaly
 201 record extends only until 2016, whereas in the Northern Hemisphere it continues through 2023.

202 For GOMOS, MIPAS, and ACE-FTS, the data from the user-friendly HARMOZ (Sofieva et al., 2013) are used.
 203 HARMOZ consists of the original retrieved ozone profiles from each instrument, screened for invalid data by the instrument
 204 experts and presented on a common vertical grid and in a common netCDF4 format, which simplifies the data usage. Below
 205 are more detailed descriptions of the individual datasets.

206

207 **Table 1: Description of datasets included in the METEOR-O₃.**

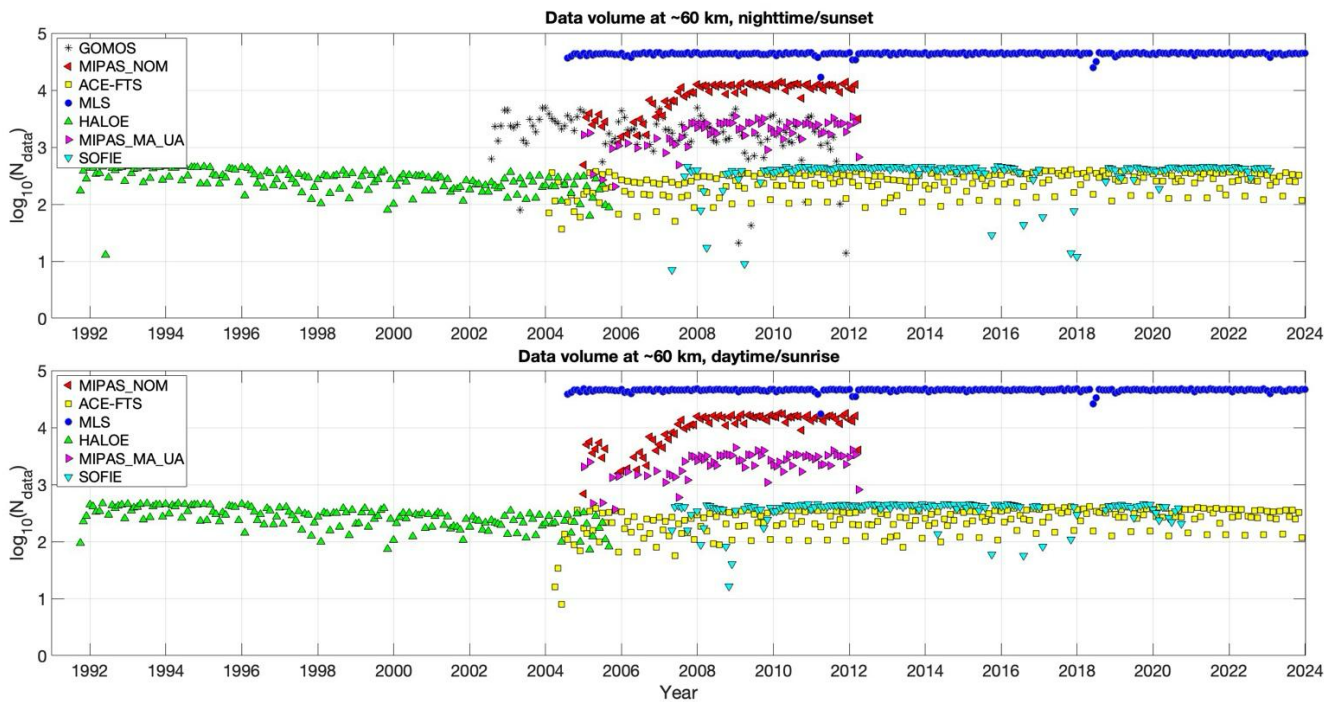
Dataset name	Satellite/ processor	Time period	Illumination conditions	Vertical range/ retrieval coordinate	Vertical resolution	Latitude coverage
HALOE	UARS/ v19	Sep 1991 – Nov 2005	sunrise sunset	~45-0.001 hPa* / pressure	~2 km	~monthly global
GOMOS	ENVISAT/ ALGOM 2s v1	Aug 2002 – Dec 2011	nighttime	~22-100 km / altitude	3 km	~weekly global
MIPAS_NOM	Envisat KIT/	Jan 2005 – Apr 2012	daytime nighttime	~22-70 km/ altitude	~3-5 km	daily global

	IAA v8					
MIPAS_MA_UA	Envisat KIT/ IAA v8	Jan 2005 – Apr 2012	daytime nighttime	~22-100 km/ altitude	~3-5 km	daily global
ACE-FTS	SCISAT/ v5.2	Feb 2004 – Dec 2023	sunrise sunset	~22-95 km / altitude	~3-4 km	~monthly global, best at mid- latitudes
MLS	Aura/ NASA v5	Aug 2004 – Dec 2023	daytime nighttime	~45-0.001 hPa*/ pressure	~3-7 km	daily global
SOFIE	AIM/ v1.3	Apr 2007 - Mar 2023	sunrise sunset	~35-100 km/ altitude	~2 km	high latitudes (65-85°)

*Corresponding to ~22-95 km altitude

208

209



210

211 **Figure 1: Monthly data volume (logarithm of number of measurements) at 60 km. Top panel: nighttime/sunset**
212 **measurements, bottom panel: daytime/sunrise measurements.**

213 3 Preparation and selection of data for merging

214 Since the data in the longest dataset with dense sampling, MLS, are retrieved on a pressure grid, pressure was selected
215 as the vertical coordinate. HALOE ozone profiles are also retrieved on a pressure grid. MIPAS (both datasets), ACE-FTS and
216 SOFIE ozone profiles are retrieved on a geometric altitude grid, but temperature and pressure profiles are also retrieved from
217 the measurements, so the conversion to a pressure grid is straightforward. GOMOS provides ozone number density profiles
218 on an altitude grid. Since the temperature and pressure profiles provided in the GOMOS files rely on a combination of ECMWF
219 analyses and the MSIS90 model (Mass Spectrometer–Incoherent Scatter model; Hedin 1983, 1991) and are therefore not very
220 accurate, we used an altitude-pressure relationship derived from MIPAS_MA_UA measurements to convert the GOMOS
221 profiles (registered in altitude) to a pressure grid. The GOMOS mixing ratios are computed consistently with the altitude-
222 pressure-density conversion (see detailed description in the Supplement).

223 For creating monthly zonal-mean data from the individual datasets, 10° latitude bands from 80°S to 80°N are used. The
224 specific challenge for combining ozone data in the mesosphere is that measurements are made at different local times, while
225 diurnal variations are large in the MLT. Therefore, we first computed monthly zonal-mean ozone profiles for each illumination
226 condition: daytime (solar zenith angle <90°), nighttime (solar zenith angle >108°), sunset or sunrise. For MLS and MIPAS
227 make daytime and nighttime measurements, HALOE, ACE-FTS and SOFIE measure at sunset and sunrise.

228 For all datasets, the monthly zonal average is computed as the mean of ozone profiles $x_k(t, z, \theta, l)$, for each illumination
229 condition l (daytime, nighttime, sunset, sunrise), month t , pressure level z and latitude band θ :

$$230 \quad \rho(t, z, \theta, l) = \frac{1}{N_t} \sum x_k(t, z, \theta, l), \quad (1)$$

231 where N_t is the number of measurements available in month t . We required $N_t > 10$ in computation of monthly zonal-
232 mean values. The uncertainty of the monthly mean $\sigma_\rho^2(t, z, \theta, l)$ can be estimated as the standard error of the mean:

$$233 \quad \sigma_\rho^2(t, z, \theta, l) = \frac{s^2(t, z, \theta, l)}{N_t}, \quad (2)$$

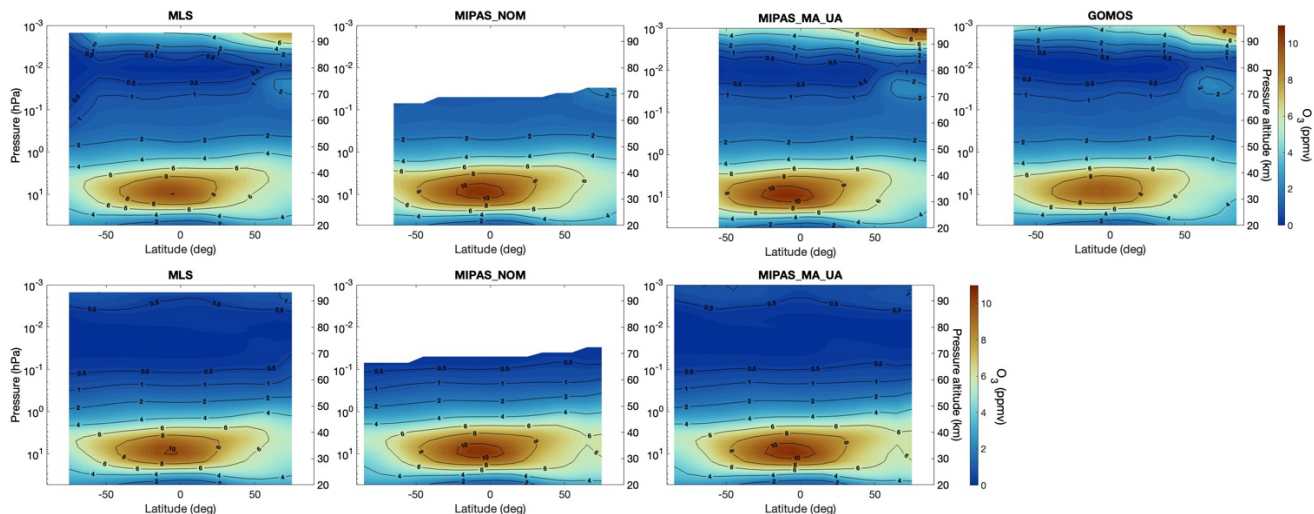
234 where $s^2(t, z, \theta, l)$ is the sample variance. In Eq. (2), we used a robust estimator for the sample variance, i.e., $s = 0.5(P_{84} -$
235 $P_{16})$, where P_{84} and P_{16} are the 84th and 16th percentiles of the distribution, respectively, similarly to the approach taken by
236 Sofieva et al. (2017).

237 To assess dataset consistency prior to merging, Figures 2-3 demonstrate how well the various individual datasets
238 reproduce the vertical structure and diurnal behaviour of ozone in the stratosphere and MLT. The monthly zonal-mean boreal
239 wintertime (DJF) ozone distributions for MLS, MIPAS_NOM, MIPAS_MA_UA and GOMOS are presented in Figure 2. The
240 averaged values were calculated for the period 2005-2011 for these datasets. This period was chosen for intercomparison

241 purposes, as it represents a time window with overlapping observations from MLS, MIPAS_NOM, MIPAS_MA_UA, and
 242 GOMOS. The top panel shows nighttime conditions, while the bottom panel represents daytime. Pressure altitudes are
 243 computed from pressure as $z = 16 \log_{10}(1013/P)$, where P is pressure in hPa. This pressure-derived altitude coordinate is
 244 used throughout the manuscript.

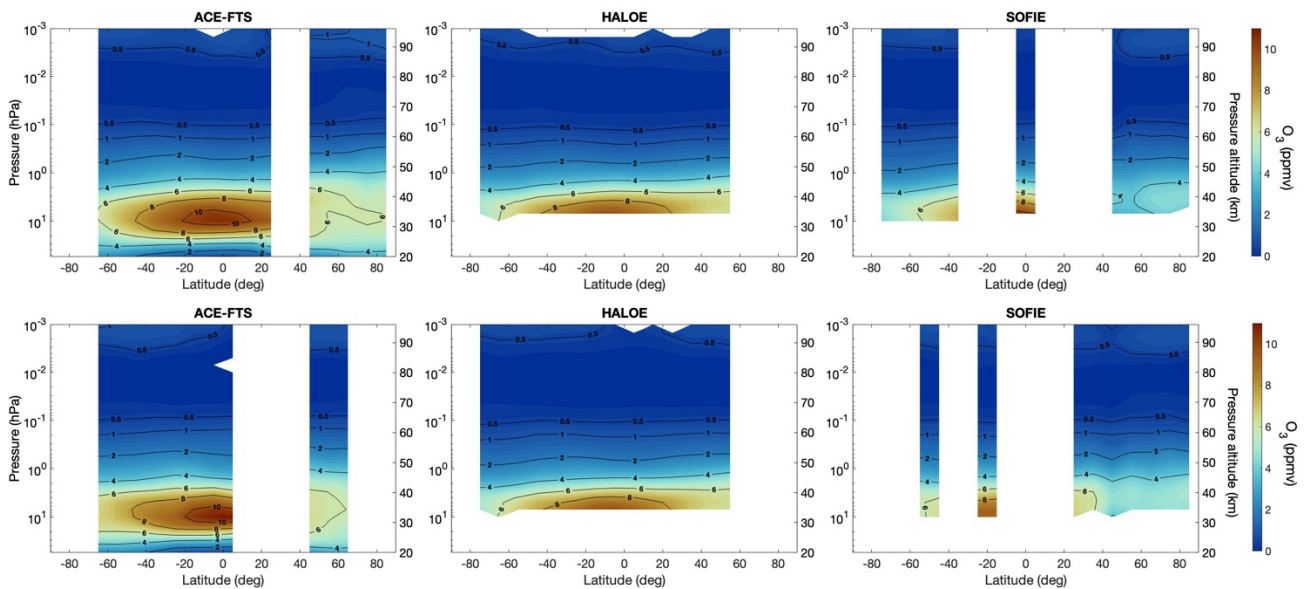
245 Across datasets, ozone distributions are similar, highlighting well-defined features. The nighttime ozone vertical
 246 distribution (top panels in Fig. 2) exhibits three distinct maxima. The primary ozone maximum occurs in the stratosphere,
 247 between approximately 30 and 35 km, where ozone mixing ratios reach about 10-11 ppmv (maximum in the tropics). It is
 248 produced through a photochemical equilibrium involving oxygen molecules, atomic oxygen, and solar ultraviolet radiation,
 249 and is modulated by natural variability and human activities (e.g. ozone-depleting substances, NO_x cycle; Brasseur and
 250 Solomon, 2005). The secondary maximum is found around 90-95 km, with the nighttime values as high as the stratospheric
 251 maxima (~10 ppmv). The secondary ozone peak represents a short-lived photochemical equilibrium strongly influenced by
 252 temperature and by the concentrations of atomic hydrogen and atomic oxygen (Smith and Marsh, 2005). During polar winter,
 253 a tertiary ozone maximum of roughly 2-3 ppmv develops near 72 km, peaking close to the polar night terminator. This feature
 254 results from reduced concentrations of odd hydrogen during nighttime, decreasing odd-oxygen losses via HO_x catalytic cycles
 255 (e.g., Marsh et al., 2001; Sofieva et al., 2009).

256 In the middle and lower stratosphere, ozone exhibits relatively small diurnal variations because atomic oxygen
 257 concentrations are small compared to ozone, and ozone lifetimes exceed one day. As altitude increases into the MLT, diurnal
 258 variations become stronger. They are mainly controlled by the daytime photolysis of ozone and its reformation at night through
 259 the recombination of atomic and molecular oxygen. The efficiency of ozone production increases with altitude as atomic
 260 oxygen becomes more abundant (Brasseur and Solomon, 2005).



261
 262 **Figure 2: Boreal wintertime (DJF) zonal-mean ozone profiles for the years 2005-2011 for MLS, MIPAS_NOM, MIPAS_MA_UA**
 263 **and GOMOS (from left to right) for nighttime (top) and daytime (bottom) measurements.**

264 Figure 3 presents the monthly zonal-mean ozone distributions for boreal winter (DJF) as measured by the occultation
 265 instruments ACE-FTS, HALOE, and SOFIE. The DJF means were calculated for the periods 2005-2011 for ACE-FTS, 1991-
 266 2005 for HALOE, and 2007-2023 for SOFIE. Selecting 2005-2011 as the common period (as done for the limb measurements)
 267 is not possible here, because the time spans of the solar occultation instruments differ. Only ACE-FTS overlaps with this
 268 period, whereas HALOE and SOFIE operate largely outside it. Therefore, HALOE and SOFIE climatologies are shown for
 269 their full available periods, while ACE-FTS is presented for 2005–2011, consistent with Figure 2. For the most part, similar
 270 features are observed as in Fig. 2. The ozone distributions show good consistency among all datasets, with spatial patterns
 271 clearly observed. However, a key difference is the nighttime ozone enhancement above 70 km. Solar occultation observations
 272 are limited to periods when the sun is rising or setting, rather than during complete darkness. The pronounced nighttime ozone
 273 enhancement in the MLT occurs during full darkness, outside the observation window of solar occultation instruments. The
 274 wintertime means from ACE-FTS and HALOE are in good agreement with those previously reported by Smith et al. (2013).



275
 276 **Figure 3: Boreal wintertime (DJF) zonal-mean ozone profiles for the years 2005-2011 for ACE-FTS, 1991-2005 for HALOE and**
 277 **2007-2023 for SOFIE (from left to right) for sunset (top) and sunrise (bottom) measurements.**

278 An example time series of nighttime ozone at northern mid-latitudes (30°N-60°N) from four instruments (MLS,
 279 MIPAS_NOM, MIPAS_MA_UA, and GOMOS), illustrating the vertical distribution of ozone over time, is shown in
 280 Supplementary Fig. S4. Temporal variations in ozone are similarly represented across datasets, with key patterns over time
 281 clearly visible. Seasonal variations in ozone primarily manifest as an annual cycle in the stratosphere, with a maximum of
 282 about 10-11 ppmv in late spring/early summer. In the MLT region, a semi-annual cycle is observed, with ozone peaks of about
 283 10-12 ppmv occurring around March-May and September-November.

284

286 4 The merging procedure

287 The merging procedure in general is like that used by Sofieva et al. (2017b, 2023) but is adapted for the MLT region
 288 by considering the strong diurnal cycle of ozone. Below we present the details of the merging procedure. It consists of three
 289 main steps: (i) evaluation of deseasonalized anomalies, (ii) data pre-merging, and (iii) final merging of pre-merged datasets
 290 from individual datasets.

291 4.1 Seasonal cycle and deseasonalized anomalies

292 For each dataset, illumination condition l , latitude band θ , and pressure level z , the climatological monthly mean ozone
 293 mixing ratio $\rho_m(z, \theta)$ (seasonal cycle) is first evaluated. The seasonal cycle is obtained by averaging the monthly zonal mean
 294 ozone mixing ratios over a set of selected years for a given month m :

$$295 \rho_m(z, \theta, l) = \frac{1}{N_m} \sum_{j=1}^{N_m} \rho_j(z, \theta, l), \quad (3)$$

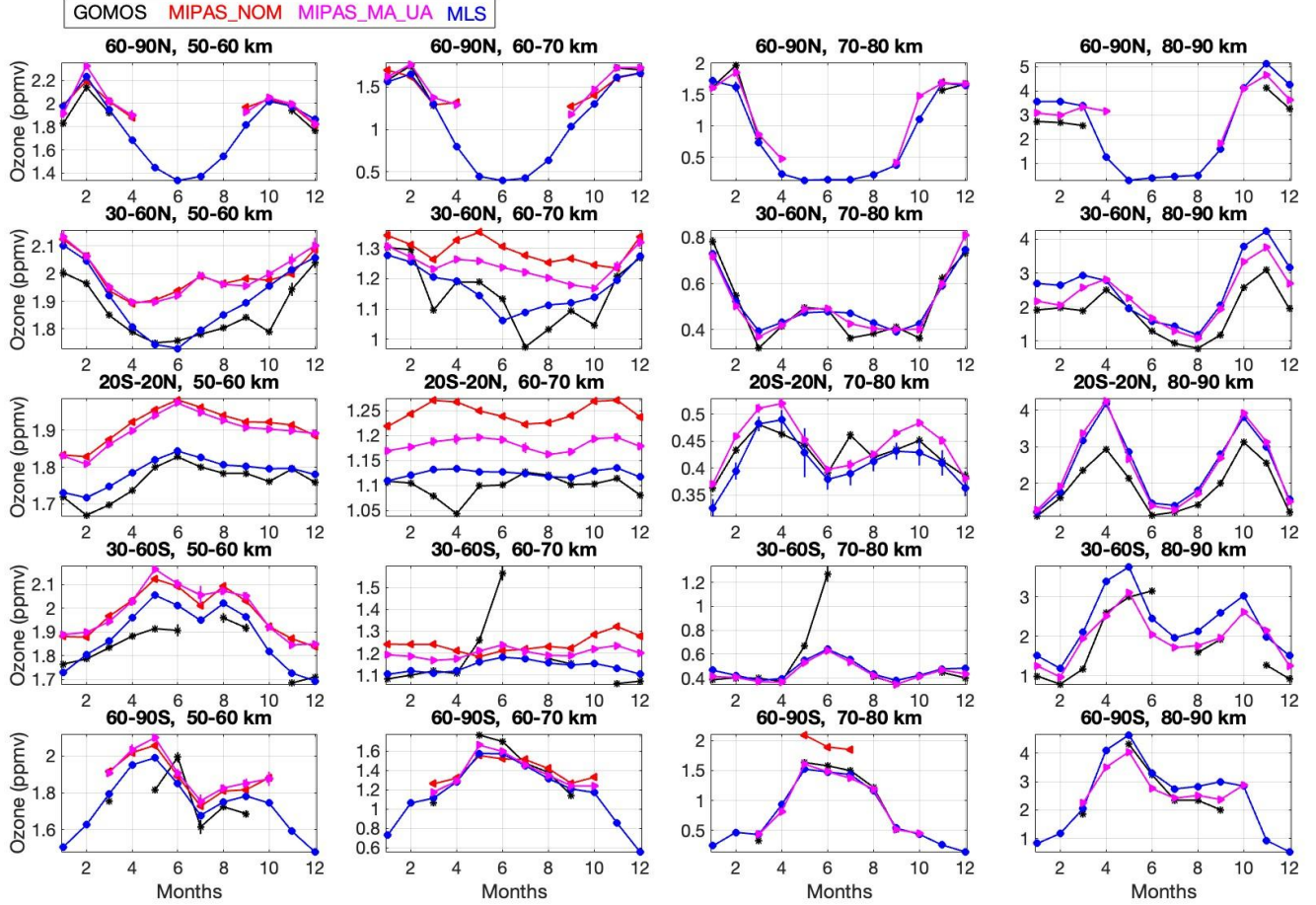
296 where $\rho_j(z, \theta, l)$ is the monthly zonal mean ozone mixing ratio for month m in year j , and N_m is the number of selected
 297 years. For GOMOS, MIPAS_NOM, MIPAS_MA_UA, and MLS, the seasonal cycle is evaluated over the common operational
 298 period 2005-2011, ensuring consistency in the computation of median deseasonalized anomalies and avoiding biases arising
 299 from the use of different reference periods. For ACE-FTS, the seasonal cycle is derived from 2005-2018 to reduce sampling-
 300 related uncertainty, assuming negligible differences between the 2005-2011 and 2005-2018 seasonal climatologies. For
 301 HALOE and SOFIE, the full operational periods are used to estimate the seasonal cycle, and their deseasonalized anomalies
 302 are adjusted to the 2005-2011 reference period during merging (see below). The uncertainty of the seasonal cycle $\rho_m(z, \theta, l)$
 303 for each month m , expressed as its variance $\sigma_m^2(z, \theta, l)$ is evaluated from uncertainties of individual monthly mean values
 304 $\sigma_{\rho,j}^2$ as

$$305 \sigma_m^2(z, \theta, l) = \frac{1}{N_m^2} \sum_{j=1}^{N_m} \sigma_{\rho,j}^2(z, \theta, l), \quad (4)$$

306 where $\sigma_{\rho,j}^2(z, \theta, l)$ is the variance of the monthly zonal mean ozone mixing ratio for month m in year j at altitude z
 307 and illumination condition l .

308 Figure 4 illustrates the climatological monthly mean $\rho_m(z, \theta, l)$ of nighttime ozone measurements for different
 309 latitude bands: 60°N-90°N, 30°N-60°N, 20°S-20°N, 30°S-60°S, and 60°S-90°S (from top to bottom), across four altitude
 310 ranges: 50-60 km, 60-70 km, 70-80 km, and 80-90 km (from left to right). The semi-annual cycle in the MLT is clearly visible,
 311 with ozone concentrations exhibiting two peaks per year during equinoxes.

312 Agreement among datasets is generally good, though some discrepancies between them exist, consistent with earlier
 313 validation and intercomparison results (Smith et al., 2013; Lopez-Puertas et al., 2023; Das et al., 2023). Additionally, GOMOS
 314 shows some biases, which can be (partially) attributed to its coarser temporal and horizontal sampling, compared to that of
 315 MLS and MIPAS (see Fig. 1 and Section 2.2).
 316



317
 318 **Figure 4: Ozone climatological monthly mean $\rho_m(z, \theta, l)$ of nighttime measurements in latitude bands 60°N-90°N, 30°N-60°N, 20°S-**
 319 **20°N, 30°S-60°S and 60°S-90°S (from top to bottom) for altitudes 50-60 km, 60-70 km, 70-80 km and 80-90 km (from left to right).**
 320 **The seasonal cycles in the indicated zones are computed as the mean of seasonal cycles in 10° latitude bands.**

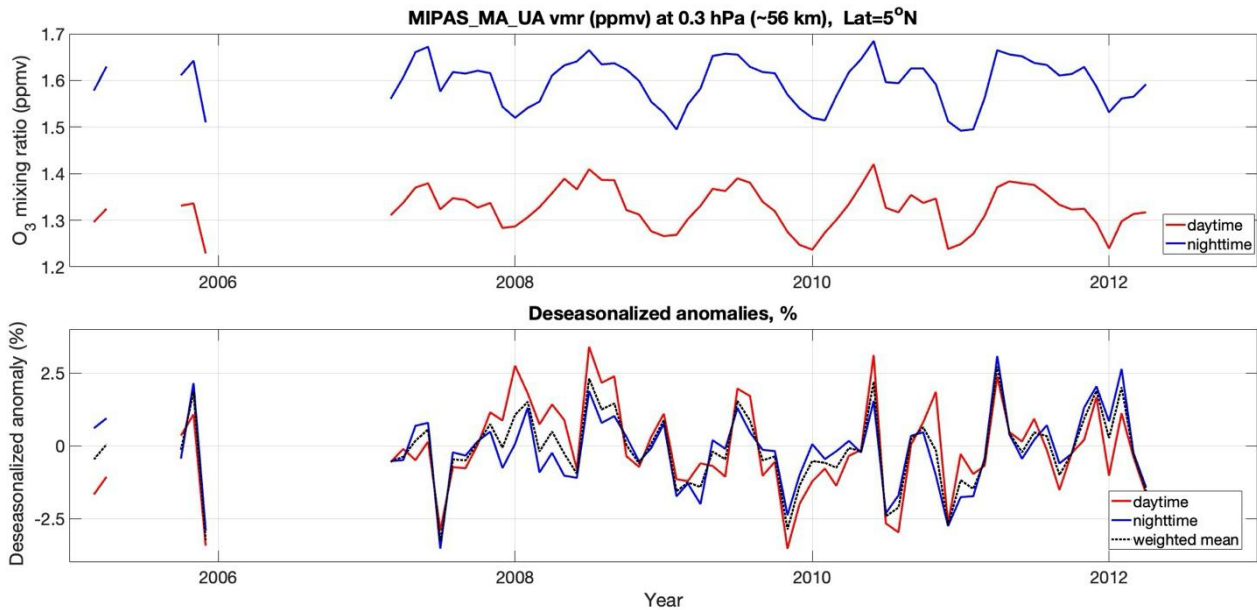
321 After evaluating the seasonal cycle, the deseasonalized ozone anomalies are computed as:

$$322 \quad \Delta(t, z, \theta, l) = \frac{\rho(t, z, \theta, l) - \rho_m(z, \theta, l)}{\rho_m(z, \theta, l)}, \quad (5)$$

323 where $\Delta(t, z, \theta, l)$ is the monthly zonal mean ozone mixing ratio at month t , latitude band θ , illumination condition l and
 324 pressure level z (defined in Eq. 1), and $\rho_m(z, \theta, l)$ is the climatological monthly mean (seasonal cycle) for the corresponding
 325 month m (defined in Eq. 3). The uncertainty of the deseasonalized anomalies is evaluated using standard error propagation for
 326 each dataset, illumination condition and latitude band.

327 4.2 Pre-merging

328 Ozone in the mesosphere exhibits strong diurnal variations, as discussed above and illustrated in Figures 2 and 3. This
 329 behaviour is also evident in the top panel of Figure 5, which shows examples of absolute ozone mixing ratios from
 330 MIPAS_MA_UA at 56 km and 5° latitude under different illumination conditions l . While the absolute ozone mixing ratios
 331 differ substantially between illumination conditions, the deseasonalized anomalies (bottom panel of Figure 5) are nearly
 332 identical for the instruments with dense sampling. The daytime, nighttime, and weighted mean deseasonalized anomalies are
 333 highly consistent across the full altitude range of the MIPAS_MA_UA measurements, as shown in Supplementary Fig. S5.
 334 This validation procedure was performed across all datasets. Because the daytime and nighttime deseasonalised anomalies are
 335 nearly identical, we combine them by taking a weighted mean, which we refer to hereafter as “pre-merged” deseasonalized
 336 anomaly from each dataset. The weights are inversely proportional to the estimated uncertainties of the deseasonalized
 337 anomalies.



338 **Figure 5: Top: ozone mixing ratio at 56 km for MIPAS_MA_UA daytime and nighttime observations in latitude zone 0-10°N.**
 339 **Bottom: the corresponding deseasonalized anomalies and the weighted mean anomaly (see text for explanation).**
 340

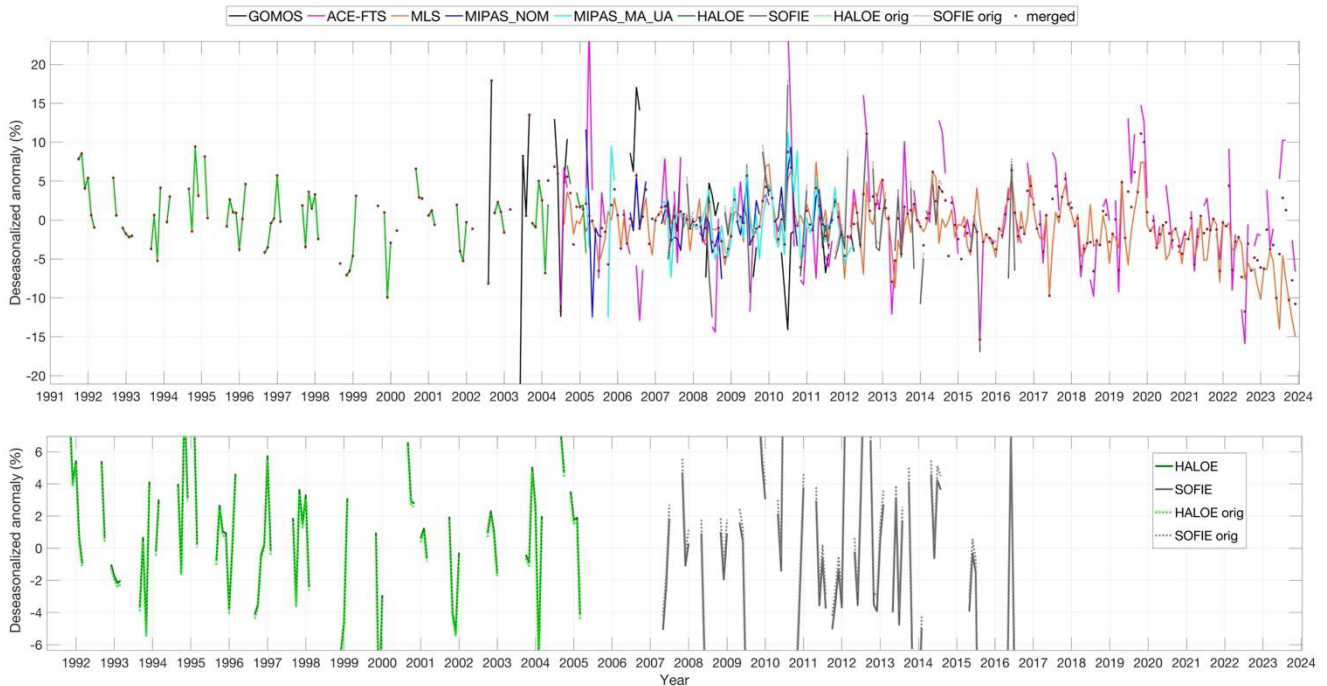
341 **4.3 The merging procedure**

342 The merging procedure is like that used for the SAGE-CCI-OMPS+ merged dataset (Sofieva et al., 2017b, 2023), and
 343 is illustrated in Fig. 6. First, we computed the merged anomaly as the median of all individual dataset anomalies, excluding
 344 HALOE and SOFIE, for each pressure level z , latitude band θ , and month t :

345
$$\Delta_{merged}(t, z, \theta) = median(\Delta_k(t, z, \theta)), \quad (6)$$

346 where $\Delta_k(t, z, \theta)$ indicates the individual dataset anomaly (top panel of Fig. 6). Next, the pre-merged HALOE and SOFIE
 347 anomalies, for which the seasonal cycles are calculated over different time periods (as explained above), are adjusted (offset)
 348 to this median anomaly. These offsets are generally very small (bottom panel of Fig. 6). Finally, the median of all aligned
 349 anomalies is computed (shown as red dots in the top panel of Fig. 6). The merging procedure is performed for each month,
 350 each latitude band, and each pressure level. An example of vertical profiles of pre-merged deseasonalized anomalies from
 351 individual datasets and the merged anomaly is shown in Figure 7 for the latitude zone 60°S-70°S. The altitude coverage slightly
 352 varies between the datasets. The best spatio-temporal coverage is attained after 2004.

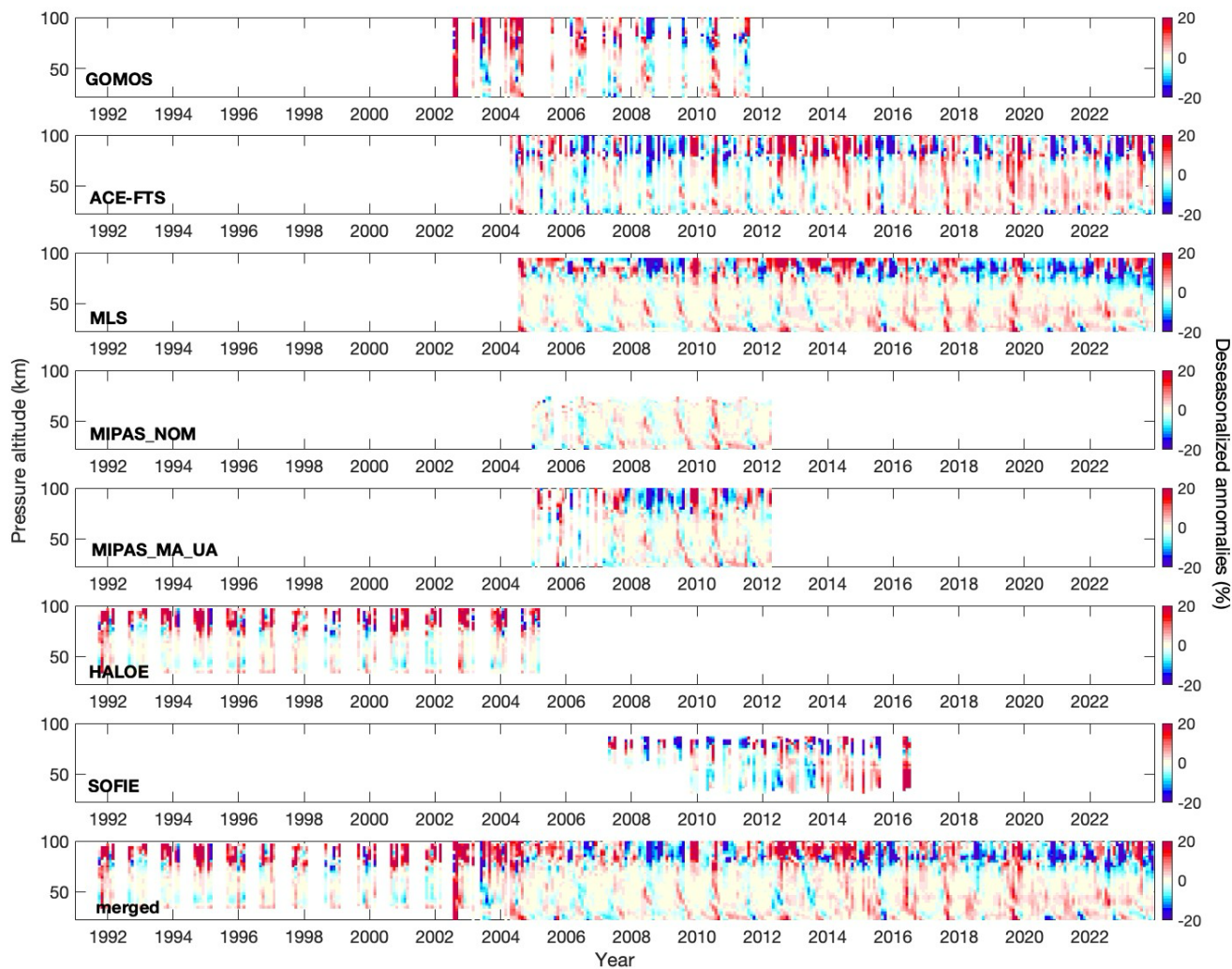
353 When performing data merging, we also analysed the deviations of individual pre-merged anomalies from the merged
 354 anomaly, to detect drifts or strong deviations. Such a comparison is shown in Figure 8. No clear drifts were observed; the pre-
 355 merged anomalies from different datasets are in good agreement with each other.



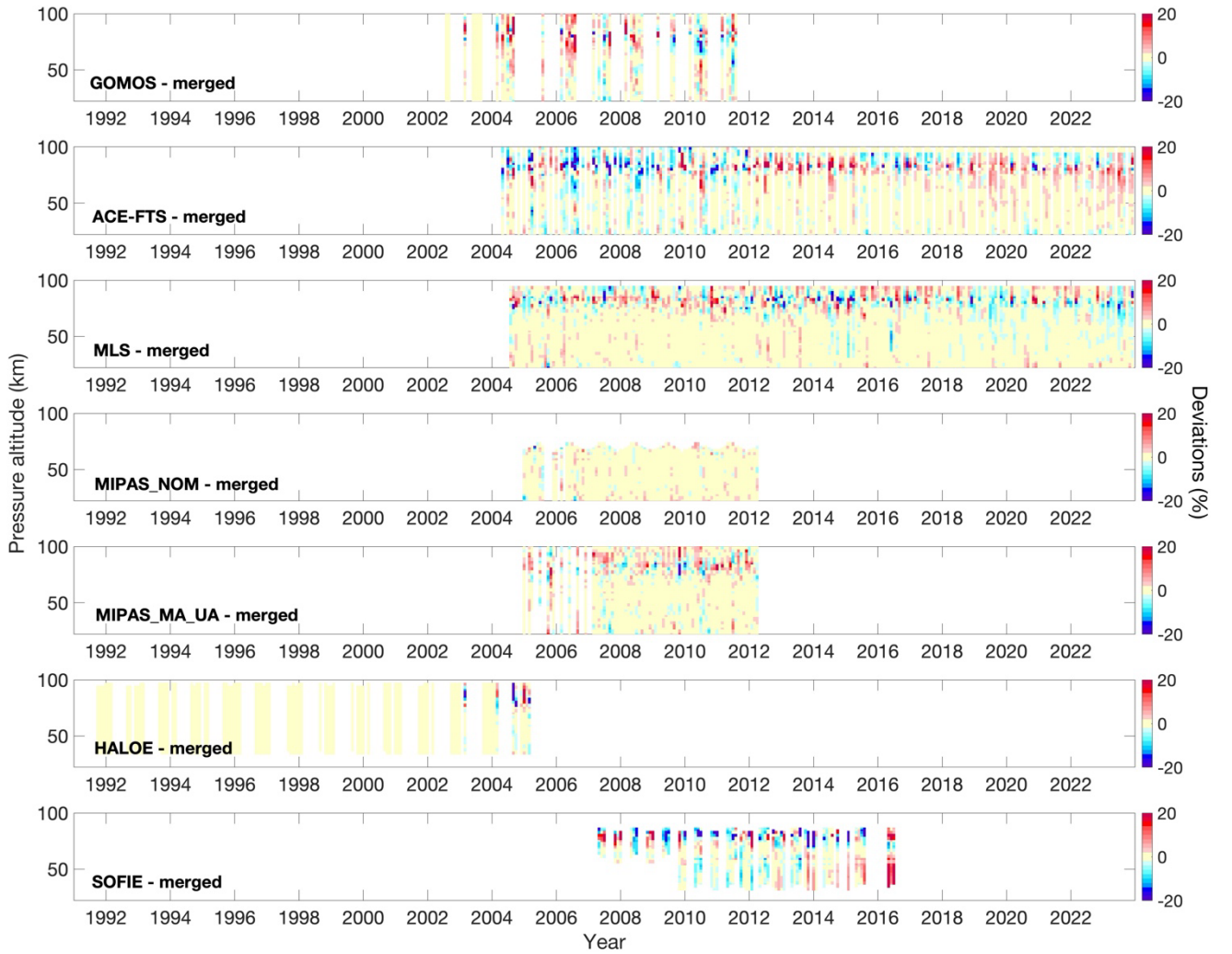
356
 357 **Figure 6: Illustration of the merging procedure using the data at 60°S-70°S, 0.05hPa. Colored lines: individual pre-merged**
 358 **deseasonalized anomalies for different datasets (see legend). For HALOE and SOFIE, the original anomalies are shown by dotted**

359 lines, while offset anomalies are shown by solid lines. The final merged anomaly is shown by dark red dots. Top: all data, bottom: a
360 zoom on HALOE and SOFIE anomalies for visualization of small offsets.

361



362
363 **Figure 7: An example of vertical profiles of pre-merged deseasonalized anomalies from individual datasets and the final merged**
364 **anomaly. The data are from the latitude zone 60°S-70°S.**



365

366

Figure 8: Example of deviations of individual deseasonalized anomalies from the merged anomaly. The data are from the latitude zone 60°S-70°S.

367

368

The uncertainties of the merged ozone anomalies are evaluated as proposed by Sofieva et al., (2017b, 2023):

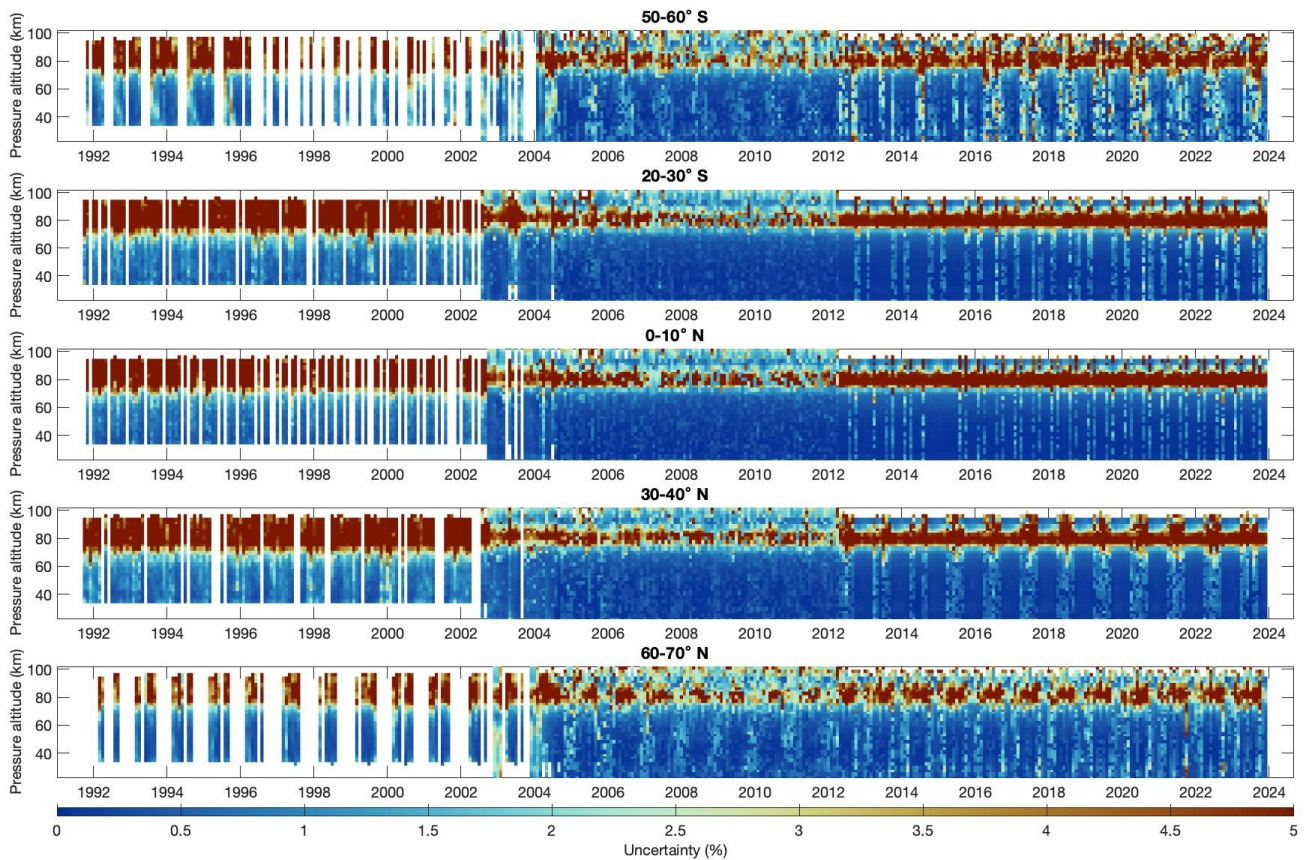
369

$$\sigma_{\Delta,merged}(t, z, \theta) = \min \left(\sigma_{\Delta,j,med}(t, z, \theta), \sqrt{\frac{1}{N} \sum_{j=1}^N \sigma_{\Delta,j}^2(t, z, \theta) + \frac{1}{N^2} \sum_{j=1}^N (\Delta_j(t, z, \theta) - \Delta_{merged}(t, z, \theta))^2} \right), \quad (7)$$

370

where $\sigma_{\Delta,j,med}(t, z, \theta)$ is the anomaly uncertainty of the dataset corresponding to the median value. The typical uncertainties of the merged deseasonalized anomalies are shown in Figure 9 for several latitude bins. In general, the estimated uncertainties are below 2%, except in the mesopause region, where they increase to 5-10%. Before 2002, when the merged record consists solely of HALOE measurements, the estimated uncertainties above 75 km are 5-10% and <2% below 70 km.

373



374

375

Figure 9: Examples of uncertainties (in %) of the merged deseasonalized anomalies. The latitude bins are indicated in the panels.

376

5 The merged METEOR-O₃ dataset of ozone profiles

377

378

379

380

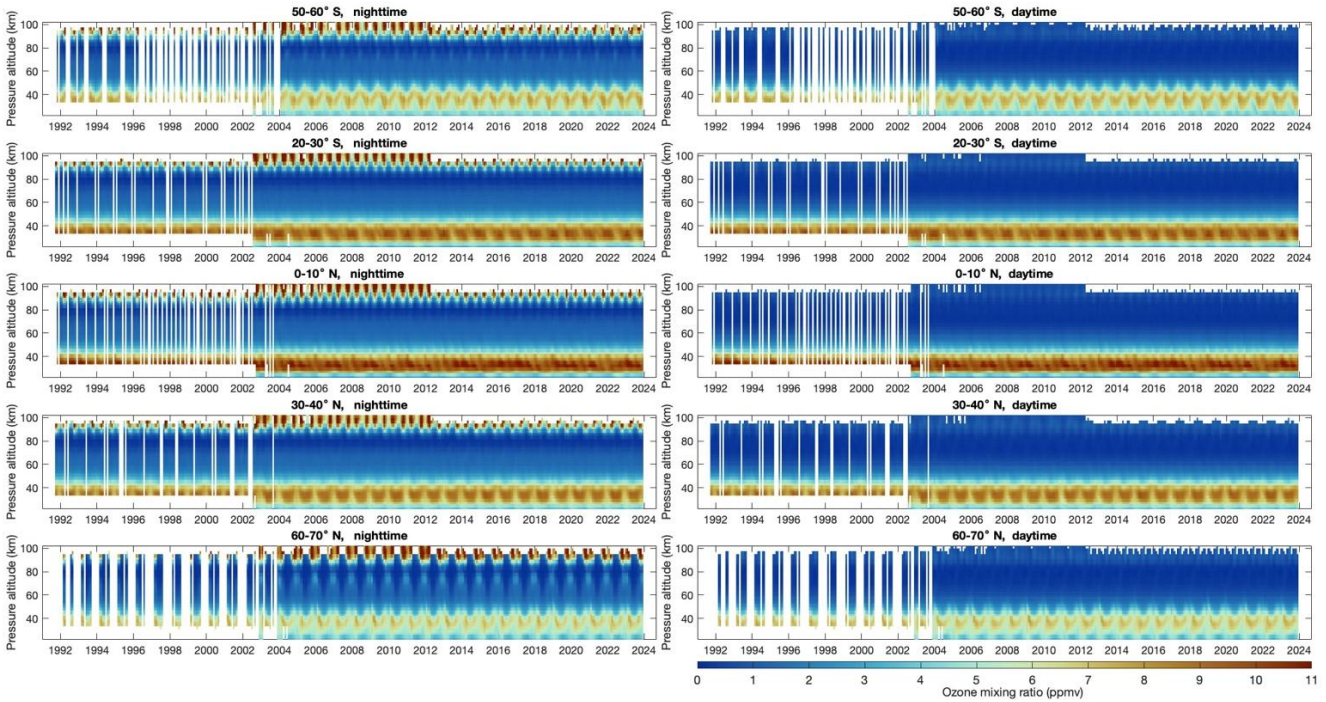
381

382

383

384

The deseasonalized anomalies can be directly used for ozone trend analyses. For other applications, we also created merged ozone mixing ratio profiles. For this purpose, we computed the merged seasonal cycle as the mean of seasonal cycles from MLS, MIPAS_NOM and MIPAS_MA_UA, for daytime and nighttime illumination conditions. These datasets were selected because of their dense sampling, and to ensure maximum spatial coverage. A similar approach is applied for the merged stratospheric ozone datasets (Sofieva et al., 2017b, 2023). This merged seasonal cycle is then applied to the merged deseasonalized anomalies. Thus, in addition to deseasonalized anomalies, nighttime and daytime ozone mixing ratio profiles and their uncertainty are provided in the merged dataset. Examples of the merged METEOR-O₃ mixing ratio profiles are shown in Figure 10.



385

386

387

Figure 10: Examples of the merged METEOR-O₃ nighttime (left) and daytime (right) time series of ozone mixing ratio profiles. The latitude bins are indicated in the panels.

388

6 Analyses of trends in the upper atmosphere

389

390

The merged deseasonalized ozone anomalies are suitable for direct use in ozone trend assessments. For this analysis, we apply a multiple linear regression (MLR) to the METEOR-O₃ dataset:

391

$$O_3(t) = PWLT(t, t_0) + q_1 QBO_{30}(t) + q_2 QBO_{50}(t) + sF_{10.7}(t) + dENSO(t), \quad (8)$$

392

393

394

395

396

397

398

399

400

where $PWLT(t, t_0)$ is a piecewise linear term (constant and a hockey-stick trend with the turnaround point in 1997), $QBO_{30}(t)$ and $QBO_{50}(t)$ are two quasi-biennial oscillation (QBO) proxies (30 hPa and 50 hPa equatorial winds; <http://www.cpc.ncep.noaa.gov/data/indices/>), $F_{10.7}(t)$ is the monthly average solar 10.7 cm radio flux (<https://www.spaceweather.gc.ca/forecast-prevision/solar-solaire/solarflux/sx-5-en.php>), and $ENSO(t)$ is the 2-month lagged El Niño–Southern Oscillation (ENSO) proxy (<https://www.esrl.noaa.gov/psd/enso/mei/data/meiv2.data>). The piecewise linear trend approach is motivated by the well-established ozone turnaround around in 1997 following the peak in ozone-depleting substances, which marks the recovery period (Harris et al., 2008). Similar formulations have been used in previous ozone trend studies (e.g., Bourassa et al., 2014; Kyrölä et al., 2013; Sofieva et al., 2017b). Uncertainties are derived from the residuals of the regression fits, and autocorrelation is corrected in both steps using the Cochrane-Orcutt transformation (Cochrane and

401 Orcutt, 1949). Trends prior to 1997 are not shown because the available record (1991-1996) is too short for a robust estimation
402 of ozone trends, particularly given the strong interannual variability in mesospheric ozone.

403 For comparison, the regression analysis was performed in two ways. In the first approach, the MLR was applied to
404 the entire merged dataset covering the period 1991-2023. In this case, the bottom altitude range was limited to the coverage of
405 HALOE observations, starting at approximately 37 km and running up to 93 km. In the second approach, the MLR was applied
406 only to the period with the best spatio-temporal coverage (2004-2023), extending from about 22 km upward. Since trend
407 estimates can be sensitive to the choice of regression period (Harris et al., 2015), this approach also serves as a robustness test
408 with respect to the selected analysis window.

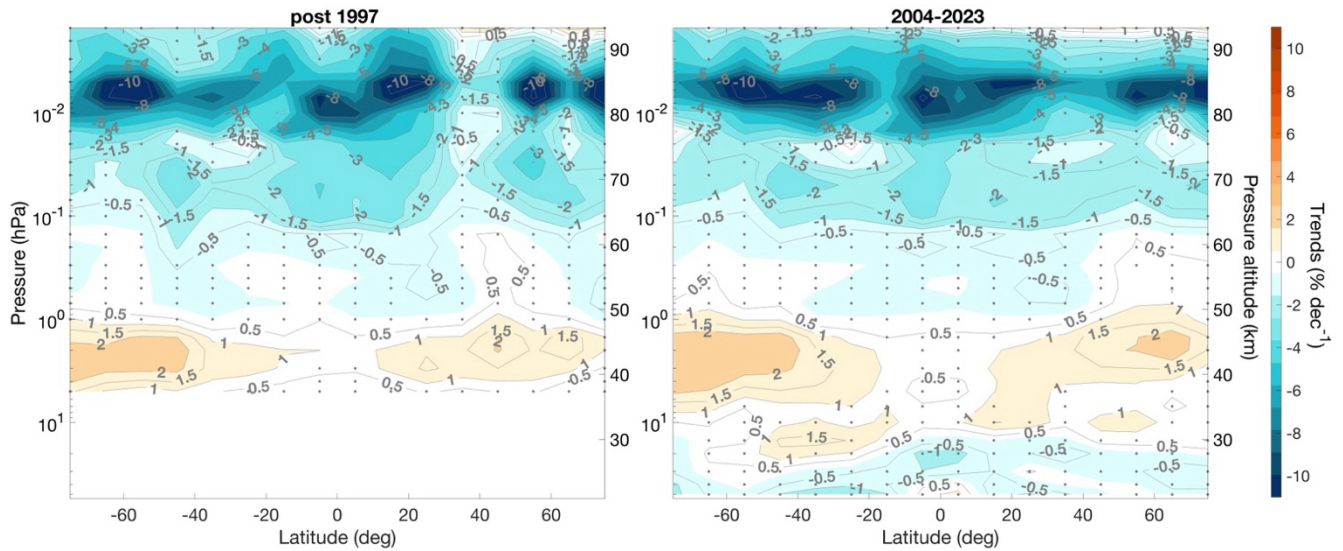
409 Figure 11 shows the trend results for the stratospheric ozone recovery period (1997-2023) and for the best spatio-
410 temporal coverage period (2004-2023). The trends are very similar for both considered periods. Stratospheric ozone trends are
411 in very good agreement with previous ozone assessments (Godin-Beekmann et al., 2022; Petropavlovskikh et al., 2019). The
412 results indicate continued recovery of ozone in the upper stratosphere, with positive values of about 1-2% per decade between
413 35 and 45 km (above the primary ozone maximum) that are particularly pronounced at middle and high latitudes in both
414 hemispheres.

415 In contrast, MLT ozone exhibits negative trends, reaching about -1 to -3% per decade over 60-80 km. The strongest
416 decreases, of approximately -8 to -12% per decade, occur between 80 and 90 km, below the secondary ozone maximum.
417 Because the trends are expressed in percent, regions with lower background ozone can exhibit larger relative changes. Previous
418 analysis based on 10 years (2002-2012) of SABER data confined to lower and middle latitudes (48°S-48°N) revealed a
419 marginally positive not-significant ozone trend at altitudes of 60-80 km and a strong negative trend up to -10% per decade
420 near 85-100 km. Positive/negative ozone trends were accompanied by a cooling trend of about -3 K per decade (Huang et al.,
421 2014). Regionally, Bizuneh et al. (2022), using 16 years of SABER data over low latitudes (5°N-15°N), have shown negative
422 temperature and ozone trends (-0.85 K per decade and -0.12 ppmv per decade) in the lower mesosphere (60-80 km) but positive
423 trends (1.25 K per decade and 0.27 ppmv per decade) in the upper mesosphere/lower thermosphere (85-100 km). Alongside
424 natural drivers, the authors attributed these patterns to the influence of increasing greenhouse gas concentrations. Furthermore,
425 rising H₂O levels in the mesosphere and lower thermosphere can enhance HO_x production, which accelerates ozone loss and
426 may further contribute to the observed negative O₃ trends.

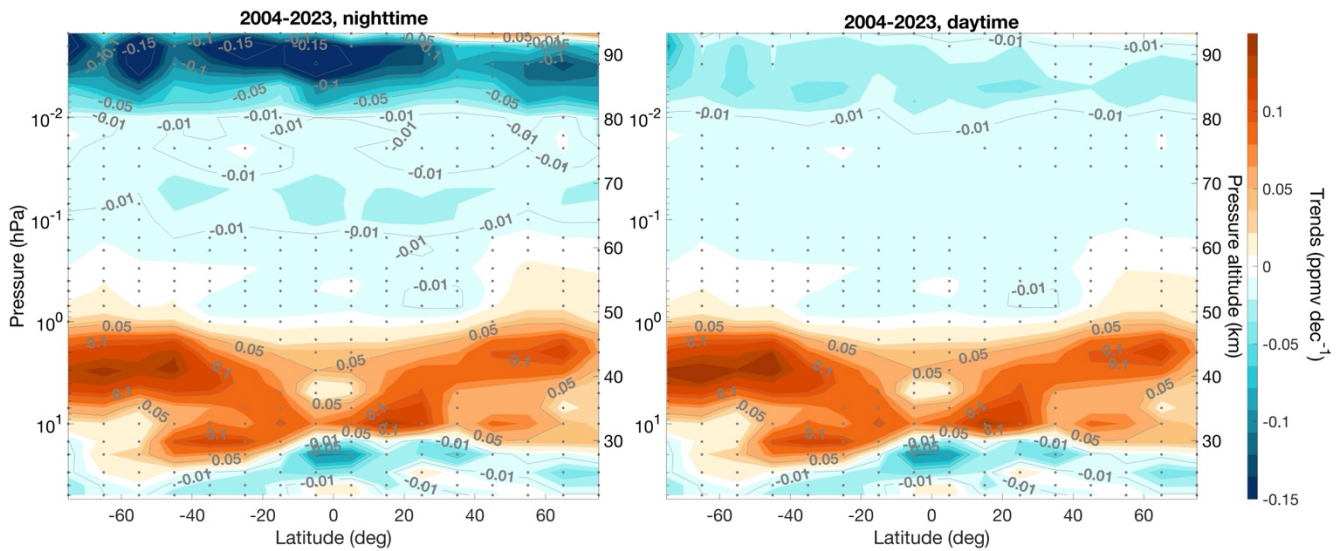
427 To assess sensitivity to the trend formulation, additional regressions were performed using the Long-term Ozone
428 Trends and Uncertainties in the Stratosphere (LOTUS) regression model (<https://usask-arg.github.io/lotus-regression/>) with an
429 independent linear term (ILT). The ILT includes two linear terms: a pre-1997 trend and a post-2000 trend. Separate intercepts
430 allow the two periods to vary independently. In contrast, the PWLT predictors impose a common value in 1997. The resulting
431 ozone trend patterns and magnitudes closely match those obtained with the original MLR (Supplementary Figure S6),
432 demonstrating that, as with the trend period, the results are also not sensitive to the chosen trend representation.

433

434 In addition to the relative (% per decade) analysis, we have also derived trends based on absolute (ppmv) ozone values
435 (Figure 12). These trends are predominantly negative between 60 and 90 km, in qualitative agreement with regional studies
436 (Bizuneh et al., 2022). In the 60-80 km range, trends vary from about -0.01 to -0.02 ppmv per decade during nighttime. At
437 altitudes above 80 km, negative trends of about -0.15 to -0.2 ppmv per decade are observed, with the peak decreases occurring
438 close to the secondary ozone maximum during nighttime. At northern mid-latitudes above 90 km, the trends weaken and in
439 some regions transition to slightly positive values, reaching up to 0.05 ppmv per decade during nighttime.



440
441 **Figure 11: Latitude-altitude variation of ozone trends derived from the METEOR-O₃ dataset. The left panel shows trends for 1997-**
442 **2023, and the right panel shows trends for 2004-2023. The black dots indicate trends that are not statistically significant at the 95%**
443 **confidence level. Trends are given in % per decade.**



444

445

Figure 12: Latitude-altitude variation of ozone trends derived from the METEOR-O₃ dataset. Trends are calculated over 2004-2023 for night (left panel) and day (right panel). The black dots denote trends that are not statistically significant at the 95% confidence level. Trends are given in ppmv per decade.

447

448

To investigate the seasonal dependence of ozone trends, we applied a two-step multiple regression technique like that described by Szelag et al. (2020). In the first step, natural cycles (solar, QBO, and ENSO) were estimated and removed from the data using the traditional MLR formulation given above (Eq. 8). The regression was performed using data from each (three-month) season separately. In the second step, the residual time series (after removal of natural variability) was used to estimate linear trends for the recovery period (2000-2023) using a simple linear regression. This two-step approach provides a robust estimation of seasonal trends by ensuring sufficient data for detecting natural cycles and by fitting linear trends only within periods where ozone changes are approximately linear.

449

450

451

452

453

454

455

Variations of ozone trends over the period 2000-2023 for each latitude and altitude are shown for each season separately in Figure 13. In the upper stratosphere, ozone trends are positive throughout all seasons and across most latitudes, consistent with previous studies (Szelag et al., 2020). The strongest positive trends, up to about 2-4% per decade, are observed at middle and high latitudes.

456

457

458

459

In the lowermost mesosphere (50-60 km), ozone trends are generally close to zero, with most not statistically significant, suggesting little long-term change in this region. Between approximately 60 and 80 km, negative trends (about -2 to -4% per decade) dominate, indicating a persistent decrease in mesospheric ozone. The largest negative values, reaching up to -15 to -20% per decade, occur between 80 and 90 km, particularly in the Northern Hemisphere during boreal summer (JJA) and in the Southern Hemisphere during austral summer (DJF) where the ozone absolute values are very low. During the equinoctial seasons, negative ozone trends peak at mid-latitudes and in the tropics. In some seasons and latitude bands, however, trends become positive, for example during local winter between 75-80 km and 60-80° latitudes.

460

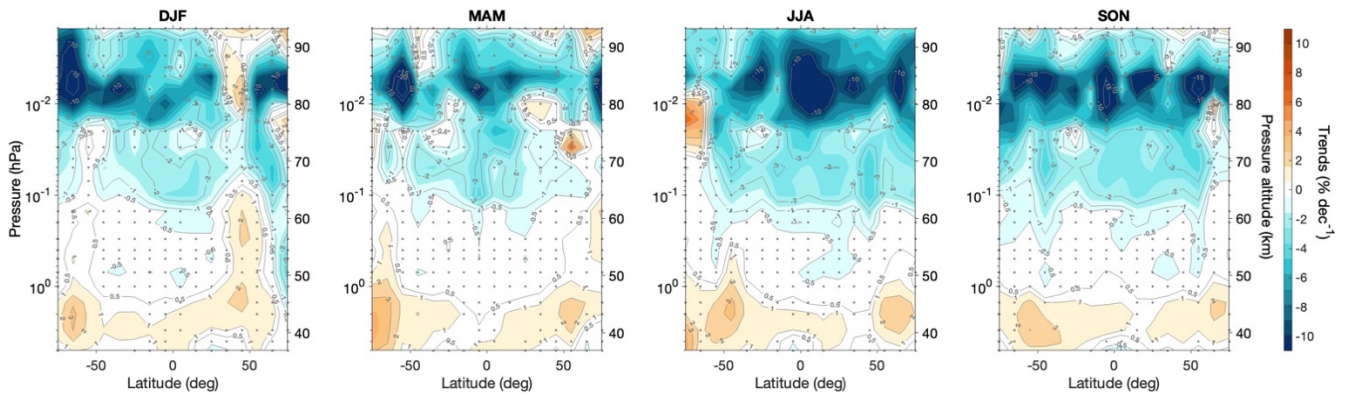
461

462

463

464

465



466

467 **Figure 13: Latitude–altitude distribution of ozone trends derived from the METEOR-O₃ dataset for each season (DJF, MAM, JJA,**
 468 **SON) over the period 2000–2023. The black dots denote trends that are not statistically significant at the 95% confidence level.**
 469 **Trends are given in % per decade.**

470 7 Summary

471 We have developed a new merged dataset of middle atmospheric ozone (~22 km to 100 km), METEOR-O₃, constructed
 472 from multiple limb emission and occultation satellite instruments (HALOE, MLS, ACE-FTS, MIPAS, GOMOS, and SOFIE).
 473 The merging procedure, adapted from previous methods for stratospheric datasets, accounts for the strong diurnal variability
 474 of ozone in the mesosphere. The dataset provides monthly zonal-mean ozone anomalies from 1991 to 2023, with 10° latitude
 475 resolution and vertical coverage from approximately 22 km up to 100 km.

476 The merged dataset shows excellent internal consistency among datasets and provides robust coverage of the middle and
 477 upper atmosphere, with typical uncertainties below 2% and slightly higher uncertainties (5–10%) near the mesopause. The
 478 deseasonalized anomalies derived from METEOR-O₃ are well suited for direct use in trend analyses.

479 Ozone trend evaluation was carried out on pressure levels using two complementary regression methods. The one-step
 480 MLR analysis was applied to the full merged dataset (1991–2023) and to the period of best spatio-temporal coverage (2004–
 481 2023). For the full-period analysis, only post-recovery (post-1997) trends were presented. The results show positive trends of
 482 about 1–2% per decade in the upper stratosphere (35–45 km), consistent with the ongoing ozone recovery observed in earlier
 483 studies (Godin-Beekmann et al., 2022; Petropavlovskikh et al., 2019). In the mesosphere, ozone trends are negative, with
 484 values of approximately -1 to -3% per decade in the 60–80 km region and up to -8 to -12% per decade between 80 and 90 km.
 485 While previous SABER-based studies were temporally and regionally limited (e.g., Bizunch et al., 2022; Huang et al., 2014),
 486 the present analysis extends to a global scale, providing for the first time a comprehensive assessment of long-term
 487 mesospheric/lower thermospheric ozone variability.

488 The METEOR-O₃ dataset enables global evaluation of long-term changes and seasonal variations. It offers a valuable
489 resource for model validation and for improving understanding of upper atmospheric processes.

490 **Code and data availability**

491 The merged METEOR-O₃ ozone dataset is publicly available from <https://fmi.b2share.csc.fi/records/jxst3-8h654>. Updates of
492 the merged dataset will be provided as more recent data become available.

493

494 **Author contributions**

495 MES and VFS designed the study, performed the analyses and wrote the manuscript. All authors provided data and
496 contributed to the analyses and writing of the paper.

497

498 **Competing interests.**

499 At least one of the (co-)authors is a member of the editorial board of Atmospheric Chemistry and Physics.

500

501 **Acknowledgments**

502 The work at Finnish Meteorological Institute has been performed within the framework of the ESA METEOR project
503 (contract 4000145342/24/I-DT-bgh). Work at the Jet Propulsion Laboratory, California Institute of Technology, was carried
504 out under a contract with the National Aeronautics and Space Administration (80NM0018D0004). The IAA team
505 acknowledges financial support from the Agencia Estatal de Investigación, MCIN/AEI/10.13039/501100011033, through
506 grants PID2022-141216NB-I00 and CEX2021-001131-S.

507 **References**

508 Bailey, S. M., Thurairajah, B., Hervig, M. E., Siskind, D. E., Russell III, J. M., and Gordley, L. L.: Trends in the polar summer
509 mesosphere temperature and pressure altitude from satellite observations, *J. Atmos. Sol.-Terr. Phys.*, 220, 105650,
510 <https://doi.org/10.1016/j.jastp.2021.105650>, 2021.

511

512 Baumgaertner, A. J. G., Seppälä, A., Jöckel, P., and Clilverd, M. A.: Geomagnetic activity related NO_x enhancements and
513 polar surface air temperature variability in a chemistry climate model: modulation of the NAM index, *Atmos. Chem. Phys.*,
514 11, 4521–4531, <https://doi.org/10.5194/acp-11-4521-2011>, 2011.

515 Bernath, P. F., McElroy, C. T., Abrams, M. C., Boone, C. D., Butler, M., Camy-Peyret, C., Carleer, M., Clerbaux, C., Coheur,
516 P.-F., Colin, R., DeCola, P., DeMazière, M., Drummond, J. R., Dufour, D., Evans, W. F. J., Fast, H., Fussen, D., Gilbert, K.,
517 Jennings, D. E., Llewellyn, E. J., Lowe, R. P., Mahieu, E., McConnell, J. C., McHugh, M., McLeod, S. D., Michaud, R.,
518 Midwinter, C., Nassar, R., Nichitiu, F., Nowlan, C., Rinsland, C. P., Rochon, Y. J., Rowlands, N., Semeniuk, K., Simon, P.,
519 Skelton, R., Sloan, J. J., Soucy, M.-A., Strong, K., Tremblay, P., Turnbull, D., Walker, K. A., Walkty, I., Wardle, D. A.,

- 520 Wehrle, V., Zander, R., and Zou, J.: Atmospheric Chemistry Experiment (ACE): Mission overview, *Geophys. Res. Lett.*, **32**,
521 L15S01, <https://doi.org/10.1029/2005GL022386>, 2005.
- 522 Bernath, P. F.: The Atmospheric Chemistry Experiment (ACE), *J. Quant. Spectrosc. Radiat. Transf.*, **186**, 3–16,
523 <https://doi.org/10.1016/j.jqsrt.2016.04.006>, 2017.
- 524 Bertaux, J.-L., Kyrölä, E., Fussen, D., Hauchecorne, A., Dalaudier, F., Sofieva, V. F., Tamminen, J., Vanhellemont, F.,
525 D’Andon, O. F., Barrot, G., Mangin, A., Blanot, L., Lebrun, J. C., Pérot, K., Fehr, T., Saavedra, L., Leppelmeier, G. W., and
526 Fraisse, R.: Global ozone monitoring by occultation of stars: an overview of GOMOS measurements on ENVISAT, *Atmos.*
527 *Chem. Phys.*, **10**, 12091–12148, <https://doi.org/10.5194/acp-10-12091-2010>, 2010.
- 528 Bhatt, P. P., Remsberg, E. E., Gordley, L. L., McInerney, J. M., Brackett, V. G., and Russell, J. M.: An evaluation of the
529 quality of Halogen Occultation Experiment ozone profiles in the lower stratosphere, *J. Geophys. Res.-Atmos.*, **104**, 9261–
530 9275, <https://doi.org/10.1029/1999JD900058>, 1999.
- 531 Bizuneh, C. L., Jaya Prakash Raju, U., Nigussie, M., and Santos, C. A. G.: Long-term temperature and ozone response to
532 natural drivers in the mesospheric region using 16 years (2005–2020) of TIMED/SABER observation data at 5–15°N, *Adv.*
533 *Space Res.*, **70**, 2095–2111, <https://doi.org/10.1016/j.asr.2022.06.051>, 2022.
- 534 Boone, C. D., Nassar, R., Walker, K. A., Rochon, Y., McLeod, S. D., Rinsland, C. P., Bernath, P. F.: Retrievals for the
535 atmospheric chemistry experiment Fourier-transform spectrometer, *Appl. Opt.*, **44**, 7218-7231,
536 <https://doi.org/10.1364/ao.44.007218>, 2005.
- 537 Boone, C. D., Bernath, P. F., and Lecours, M.: Version 5 retrievals for ACE-FTS and ACE-imagers, *J. Quant. Spectrosc.*
538 *Radiat. Transf.*, **310**, 108749, <https://doi.org/10.1016/j.jqsrt.2023.108749>, 2023.
- 539 Bourassa, A. E., Degenstein, D. A., Randel, W. J., Zawodny, J. M., Kyrölä, E., McLinden, C. A., Sioris, C. E., and Roth, C.
540 Z.: Trends in stratospheric ozone derived from merged SAGE II and Odin-OSIRIS satellite observations, *Atmos. Chem. Phys.*,
541 **14**, 6983–6994, <https://doi.org/10.5194/acp-14-6983-2014>, 2014.
- 542 Brasseur, G. P. and Solomon, S.: *Aeronomy of the middle atmosphere*, Springer, Dordrecht, The Netherlands, 2005.
- 543 Cnossen, I.: Analysis and attribution of climate change in the upper atmosphere from 1950 to 2015 simulated by WACCM-X.
544 *J. Geophys. Res.-Space Phys.*, **125**(12), <https://doi.org/10.1029/2020ja028623>, 2020.
- 545 Cnossen, I., Emmert, J. T., Garcia, R. R., Elias, A. G., Mlyneczek, M. G., and Zhang, S.-R.: A review of global long-term
546 changes in the mesosphere, thermosphere and ionosphere: A starting point for inclusion in (semi-) empirical models. *Adv.*
547 *Space Res.*, **74**(11), 5991–6011, <https://doi.org/10.1016/j.asr.2024.10.005>, 2024.
- 548 Cochran, D. and Orcutt, G. H.: Application of Least Squares Regression to Relationships Containing Auto-Correlated Error
549 Terms, *J. Am. Stat. Assoc.*, **44**, 32–61, <https://doi.org/10.1080/01621459.1949.10483290>, 1949.
- 550 Das, U.: Spatial variability in long-term temperature trends in the middle atmosphere from SABER/TIMED observations, *Adv.*
551 *Space Res.*, **68**, 2890–2903, <https://doi.org/10.1016/j.asr.2021.05.014>, 2021.

- 552 Das, S., Bailey, S. M., Hervig, M. E., Thuraiajah, B., and Marshall, B. T.: Validation of Version 1.3 Ozone Measured by the
553 SOFIE Instrument, *Earth Space Sci.*, 10, e2022EA002649, <https://doi.org/10.1029/2022EA002649>, 2023.
- 554 Fischer, H., Birk, M., Blom, C., Carli, B., Carlotti, M., von Clarmann, T., Delbouille, L., Dudhia, A., Ehhalt, D., Endemann,
555 M., Flaud, J. M., Gessner, R., Kleinert, A., Koopman, R., Langen, J., López-Puertas, M., Mosner, P., Nett, H., Oelhaf, H.,
556 Perron, G., Remedios, J., Ridolfi, M., Stiller, G., and Zander, R.: MIPAS: an instrument for atmospheric and climate research,
557 *Atmos. Chem. Phys.*, 8, 2151–2188, <https://doi.org/10.5194/acp-8-2151-2008>, 2008.
- 558 Godin-Beekmann, S., Azouz, N., Sofieva, V. F., Hubert, D., Petropavlovskikh, I., Effertz, P., Ancellet, G., Degenstein, D. A.,
559 Zawada, D., Froidevaux, L., Frith, S., Wild, J., Davis, S., Steinbrecht, W., Leblanc, T., Querel, R., Tourpali, K., Damadeo, R.,
560 Maillard Barras, E., Stübi, R., Vigouroux, C., Arosio, C., Nedoluha, G., Boyd, I., Van Malderen, R., Mahieu, E., Smale, D.,
561 and Sussmann, R.: Updated trends of the stratospheric ozone vertical distribution in the 60° S–60° N latitude range based on
562 the LOTUS regression model, *Atmos. Chem. Phys.*, 22, 11657–11673, <https://doi.org/10.5194/acp-22-11657-2022>, 2022.
- 563 Gordley, L., Burton, J., Marshall, B. T., McHugh, M., Deaver, L., Nelsen, J., Russell, J. M., and Bailey, S.: High precision
564 refraction measurements by solar imaging during occultation: results from SOFIE, *Appl. Opt.*, 48, 4814,
565 <https://doi.org/10.1364/AO.48.004814>, 2009a.
- 566 Gordley, L. L., Hervig, M. E., Fish, C., Russell, J. M., Bailey, S., Cook, J., Hansen, S., Shumway, A., Paxton, G., Deaver, L.,
567 Marshall, T., Burton, J., Magill, B., Brown, C., Thompson, E., and Kemp, J.: The solar occultation for ice experiment, *J.*
568 *Atmos. Sol.-Terr. Phys.*, 71, 300–315, <https://doi.org/10.1016/j.jastp.2008.07.012>, 2009b.
- 569 Harris, N. R. P., Kyrö, E., Staehelin, J., Brunner, D., Andersen, S.-B., Godin-Beekmann, S., Dhomse, S., Hadjinicolaou, P.,
570 Hansen, G., Isaksen, I., Jrrar, A., Karpetchko, A., Kivi, R., Knudsen, B., Krizan, P., Lastovicka, J., Maeder, J., Orsolini, Y.,
571 Pyle, J. A., Rex, M., Vanicek, K., Weber, M., Wohltmann, I., Zanis, P., and Zerefos, C.: Ozone trends at northern mid- and
572 high latitudes – a European perspective, *Ann. Geophys.*, 26, 1207–1220, <https://doi.org/10.5194/angeo-26-1207-2008>, 2008.
573
- 574 Harris, N. R. P., Hassler, B., Tummon, F., Bodeker, G. E., Hubert, D., Petropavlovskikh, I., Steinbrecht, W., Anderson, J.,
575 Bhartia, P. K., Boone, C. D., Bourassa, A., Davis, S. M., Degenstein, D., Delcloo, A., Frith, S. M., Froidevaux, L., Godin-
576 Beekmann, S., Jones, N., Kurylo, M. J., Kyrölä, E., Laine, M., Leblanc, S. T., Lambert, J.-C., Liley, B., Mahieu, E., Maycock,
577 A., de Mazière, M., Parrish, A., Querel, R., Rosenlof, K. H., Roth, C., Sioris, C., Staehelin, J., Stolarski, R. S., Stübi, R.,
578 Tamminen, J., Vigouroux, C., Walker, K. A., Wang, H. J., Wild, J., and Zawodny, J. M.: Past changes in the vertical
579 distribution of ozone – Part 3: Analysis and interpretation of trends, *Atmos. Chem. Phys.*, 15, 9965–9982,
580 <https://doi.org/10.5194/acp-15-9965-2015>, 2015.
581
- 582 Hedin, A. E.: A revised thermospheric model based on mass spectrometer and incoherent scatter data: MSIS-83, *J. Geophys.*
583 *Res.-Space Phys.*, 88(A12), 10170–10188. <https://doi.org/10.1029/JA088iA12p10170>, 1983.
- 584 Hedin, A. E.: Extension of the MSIS thermosphere model into the middle and lower atmosphere, *J. Geophys. Res.-Space*
585 *Phys.*, 96(A2), 1159–1172. <https://doi.org/10.1029/90JA02125>, 1991.

- 586 Hervig, M. E., Gordley, L. L., Russell III, J. M., and Bailey, S. M.: SOFIE PMC observations during the northern summer of
587 2007, *J. Atmos. Sol.-Terr. Phys.*, 71(3–4), 331–339, <https://doi.org/10.1016/j.jastp.2008.08.010>, 2009a.
- 588 Hervig, M. E., Gordley, L. L., Stevens, M. H., Russell, J. M., III, Bailey, S. M., and Baumgarten, G.: Interpretation of SOFIE
589 PMC measurements: Cloud identification and derivation of mass density, particle shape, and particle size, *J. Atmos. Sol.-Terr.*
590 *Phys.*, 71(3–4), 316–330, <https://doi.org/10.1016/j.jastp.2008.07.009>, 2009b.
- 591 Huang, F. T., Mayr, H. G., Russell, J. M., and Mlynczak, M. G.: Ozone and temperature decadal trends in the stratosphere,
592 mesosphere and lower thermosphere, based on measurements from SABER on TIMED, *Ann. Geophys.*, 32, 935–949,
593 <https://doi.org/10.5194/angeo-32-935-2014>, 2014.
- 594 Kiefer, M., von Clarmann, T., Funke, B., García-Comas, M., Glatthor, N., Grabowski, U., Höpfner, M., Kellmann, S., Laeng,
595 A., Linden, A., López-Puertas, M., and Stiller, G. P.: Version 8 IMK–IAA MIPAS ozone profiles: nominal observation mode,
596 *Atmos. Meas. Tech.*, 16, 1443–1460, <https://doi.org/10.5194/amt-16-1443-2023>, 2023.
- 597 Kyrölä, E., Tamminen, J., Sofieva, V. F., Bertaux, J.-L., Hauchecorne, A., Dalaudier, F., Fussen, D., Vanhellemont, F.,
598 D’Andon, O. F., Barrot, G., Guirlet, M., Mangin, A., Blanot, L., Fehr, T., Saavedra de Miguel, L., and Fraisse, R.: Retrieval
599 of atmospheric parameters from GOMOS data, *Atmos. Chem. Phys.*, 10, 11881–11903, [https://doi.org/10.5194/acp-10-11881-](https://doi.org/10.5194/acp-10-11881-2010)
600 2010, 2010.
- 601 Kyrölä, E., Laine, M., Sofieva, V., Tamminen, J., Päivärinta, S.-M., Tukiainen, S., Zawodny, J., and Thomason, L.: Combined
602 SAGE II–GOMOS ozone profile data set for 1984–2011 and trend analysis of the vertical distribution of ozone, *Atmos. Chem.*
603 *Phys.*, 13, 10645–10658, <https://doi.org/10.5194/acp-13-10645-2013>, 2013.
- 604 Langematz, U., Grenfell, J. L., Matthes, K., Mieth, P., Kunze, M., Steil, B., and Brühl, C.: Chemical effects in 11-year solar
605 cycle simulations with the Freie Universität Berlin Climate Middle Atmosphere Model with online chemistry (FUB-CMAM-
606 CHEM), *Geophys. Res. Lett.*, 32, L13803, <https://doi.org/10.1029/2005GL022686>, 2005.
- 607 Laštovička, J., Akmaev, R.A., Beig, G., et al.: Global change in the upper atmosphere. *Science* 314 (5803), 1253–1254.
608 <https://doi.org/10.1126/science.1135134>, 2006a.
- 609 Laštovička, J.: A review of recent progress in trends in the upper atmosphere. *J. Atmos. Solar Terr. Phys.* 163, 2–13.
610 <https://doi.org/10.1016/j.jastp.2017.03.009>, 2017.
- 611 Laštovička, J.: Progress in investigating long-term trends in the mesosphere, thermosphere, and ionosphere, *Atmos. Chem.*
612 *Phys.*, 23, 5783–5800, <https://doi.org/10.5194/acp-23-5783-2023>, 2023.
- 613 Li, T., Yue, J., Russell III, J. M., and Zhang, X.: Long-term trend and solar cycle in the middle atmosphere temperature revealed
614 from merged HALOE and SABER datasets, *J. Atmos. Sol.-Terr. Phys.*, 212, 105506,
615 <https://doi.org/10.1016/j.jastp.2020.105506>, 2021.
- 616 Livesey, N. J., Snyder, W. V., Read, W. G., and Wagner, P. A.: Retrieval algorithms for the EOS Microwave Limb Sounder
617 (MLS), *IEEE Trans. Geosci. Remote Sens.*, 44(5), 1144–1155, <https://doi.org/10.1109/TGRS.2006.872327>, 2006.

618 Livesey, N. J., Read, W. G., Wagner, P. A., Froidevaux, L., Santee, M. L., Schwartz, M. J., et al.: Version 5.0x Level 2 and 3
619 data quality and description document, Tech. Rep. No. JPL D-105336 Rev. B, Jet Propulsion Laboratory, 2022. Retrieved
620 from <http://mls.jpl.nasa.gov>.

621 López-Puertas, M., García-Comas, M., Funke, B., von Clarmann, T., Glatthor, N., Grabowski, U., Kellmann, S., Kiefer, M.,
622 Laeng, A., Linden, A., and Stiller, G. P.: MIPAS ozone retrieval version 8: middle-atmosphere measurements, *Atmos. Meas.*
623 *Tech.*, 16, 5609–5645, <https://doi.org/10.5194/amt-16-5609-2023>, 2023.

624 Maliniemi, V., Asikainen, T., and Mursula, K.: Spatial distribution of Northern Hemisphere winter temperatures during
625 different phases of the solar cycle, *J. Geophys. Res.-Atmos.*, 119, 9752–9764, <https://doi.org/10.1002/2013JD021343>, 2014.

626 Marsh, D., Smith, A., Brasseur, G., Kaufmann, M., Grossmann, K.: The existence of a tertiary ozone maximum in the high
627 latitude middle mesosphere, *Geophys. Res. Lett.*, 28, 4531–4534, <https://doi.org/10.1029/2001GL013791>, 2001.

628 Marshall, B. T., Deaver, L. E., Thompson, R. E., Gordley, L. L., McHugh, M. J., Hervig, M. E., and Russell, J. M., III.:
629 Retrieval of temperature and pressure using broadband solar occultation: SOFIE approach and results, *Atmos. Meas. Tech.*,
630 4(5), 893–907, <https://doi.org/10.5194/amt-4-893-2011>, 2011.

631 Nath, O., and Sridharan, S.: Long-term variabilities and tendencies in zonal mean TIMED-SABER ozone and temperature in
632 the middle atmosphere at 10–15°N, *J. Atmos. Sol.-Terr. Phys.*, 120, 1–8, <https://doi.org/10.1016/j.jastp.2014.08.010>, 2014.

633 Petropavlovskikh, I., Godin-Beekmann, S., Hubert, D., Damadeo, R., Hassler, B., and Sofieva, V.: SPARC/IO3C/GAW report
634 on Long-term Ozone Trends and Uncertainties in the Stratosphere, SPARC/IO3C/GAW, SPARC Report No. 9, WCRP-
635 17/2018, GAW Report No. 241, <https://doi.org/10.17874/f899e57a20b>, 2019.

636 Qian, L., Jacobi, C., and McInerney, J. M.: Trends and solar irradiance effects in the mesosphere, *J. Geophys. Res.-Space*
637 *Phys.*, 124, 1343–1360, <https://doi.org/10.1029/2018JA026367>, 2019.

638 Qian, L., McInerney, J. M., Solomon, S. S., Liu, H., and Burns, A. G.: Climate changes in the upper atmosphere: Contributions
639 by the changing greenhouse gas concentrations and Earth’s magnetic field from the 1960s to 2010s, *J. Geophys. Res.-Space*
640 *Phys.* 126 (3), <https://doi.org/10.1029/2020ja029067>, 2021.

641 Rozanov, E., Callis, L., Schlesinger, M., Yang, F., Andronova, N., and Zubov, V.: Atmospheric response to NOy source due
642 to energetic electron precipitation, *Geophys. Res. Lett.*, 32, L14811, <https://doi.org/10.1029/2005GL023041>, 2005.

643 Rozanov, E., Calisto, M., Egorova, T., Peter, T., and Schmutz, W.: Influence of the Precipitating Energetic Particles on
644 Atmospheric Chemistry and Climate, *Surv. Geophys.*, 33, 483–501, <https://doi.org/10.1007/s10712-012-9192-0>, 2012.

645 Russell, J. M., Gordley, L. L., Park, J. H., Drayson, S. R., Hesketh, W. D., Cicerone, R. J., Tuck, A. F., Frederick, J. E., Harries,
646 J. E., and Crutzen, P. J.: The Halogen Occultation Experiment, *J. Geophys. Res.-Atmos.*, 98, 10777–10797, 1993.

647 Russell, J. M., Bailey, S. M., Gordley, L. L., Rusch, D. W., Horányi, M., Hervig, M. E., Thomas, G. E., Randall, C. E., Siskind,
648 D. E., Stevens, M. H., Summers, M. E., Taylor, M. J., Englert, C. R., Espy, P. J., McClintock, W. E., and Merkel, A. W.: The
649 Aeronomy of Ice in the Mesosphere (AIM) mission: Overview and early science results, *J. Atmos. Sol.-Terr. Phys.*, 71, 289–
650 299, <https://doi.org/10.1016/j.jastp.2008.08.011>, 2009.

- 651 Salminen, A., Asikainen, T., Maliniemi, V., and Mursula, K.: Effect of energetic electron precipitation on the northern polar
652 vortex: Explaining the QBO modulation via control of meridional circulation, *J. Geophys. Res.-Atmos.*, 124, 5807–5821,
653 <https://doi.org/10.1029/2018JD029296>, 2019.
- 654 Seppälä, A., Randall, C. E., Clilverd, M. A., Rozanov, E., and Rodger, C. J.: Geomagnetic activity and polar surface air
655 temperature variability, *J. Geophys. Res.-Space Phys.*, 114, A10312, <https://doi.org/10.1029/2008JA014029>, 2009.
- 656 Seppälä, A., Lu, H., Clilverd, M. A., and Rodger, C. J.: Geomagnetic activity signatures in wintertime stratosphere wind,
657 temperature, and wave response, *J. Geophys. Res.-Atmos.*, 118, 2169–2183, <https://doi.org/10.1002/jgrd.50236>, 2013.
- 658 Seppälä, A., Kalakoski, N., Verronen, P. T., and Szelag, M. E.: Polar mesospheric ozone loss initiates downward coupling of
659 solar signal in the Northern Hemisphere. *Nat Commun* 16, 748, <https://doi.org/10.1038/s41467-025-55966-z>, 2025.
- 660 Sheese, P. E., Boone, C. D., and Walker, K. A.: Detecting physically unrealistic outliers in ACE-FTS atmospheric
661 measurements, *Atmos. Meas. Tech.*, 8, 741–750, <https://doi.org/10.5194/amt-8-741-2015>, 2015.
- 662 Sheese, P. E., Walker, K. A., Boone, C. D., Bourassa, A. E., Degenstein, D. A., Froidevaux, L., McElroy, C. T., Murtagh, D.,
663 Russell, J. M. III, and Zou, J.: Assessment of the quality of ACE-FTS stratospheric ozone data, *Atmos. Meas. Tech.*, 15, 1233–
664 1249, <https://doi.org/10.5194/amt-15-1233-2022>, 2022.
- 665 Sinnhuber, M., Nieder, H. & Wieters, N: Energetic Particle Precipitation and the Chemistry of the Mesosphere/Lower
666 Thermosphere. *Surv Geophys* 33, 1281–1334, <https://doi.org/10.1007/s10712-012-9201-3>, 2012.
- 667 Smith, A. K. and Marsh, D. R.: Processes that account for the ozone maximum at the mesopause, *J. Geophys. Res.-Atmos.*,
668 110, 2005JD006298, <https://doi.org/10.1029/2005JD006298>, 2005.
- 669 Smith, A. K., Harvey, V. L., Mlynczak, M. G., Funke, B., García-Comas, M., Hervig, M., Kaufmann, M., Kyrölä, E., López-
670 Puertas, M., McDade, I., Randall, C. E., Russell, J. M., Sheese, P. E., Shiotani, M., Skinner, W. R., Suzuki, M., and Walker,
671 K. A.: Satellite observations of ozone in the upper mesosphere, *J. Geophys. Res.-Atmos.*, 118, 5803–5821,
672 <https://doi.org/10.1002/jgrd.50445>, 2013.
- 673 Sofieva, V. F., Tamminen, J., Haario, H., Kyrölä, E., and Lehtinen, M.: Ozone profile smoothness as a priori information in
674 the inversion from limb measurements, *Ann. Geophys.*, 22, 3411–3420, <https://doi.org/10.5194/angeo-22-3411-2004>, 2004.
- 675 Sofieva, V. F., Kyrölä, E., Verronen, P. T., Seppälä, A., Tamminen, J., Marsh, D. R., Smith, A. K., Bertaux, J.-L., Hauchecorne,
676 A., Dalaudier, F., Fussen, D., Vanhellefont, F., d’Andon, O. F., Barrot, G., Guirlet, M., Fehr, T., and Saavedra, L.: Spatio-
677 temporal observations of the tertiary ozone maximum, *Atmos. Chem. Phys.*, 9, 4439–4445, <https://doi.org/10.5194/acp-9-4439-2009>, 2009.
- 679 Sofieva, V. F., Rahpoe, N., Tamminen, J., Kyrölä, E., Kalakoski, N., Weber, M., Rozanov, A., von Savigny, C., Laeng, A.,
680 von Clarmann, T., Stiller, G., Lossow, S., Degenstein, D., Bourassa, A., Adams, C., Roth, C., Lloyd, N., Bernath, P.,
681 Hargreaves, R. J., Urban, J., Murtagh, D., Hauchecorne, A., Dalaudier, F., van Roozendaal, M., Kalb, N., and Zehner, C.:
682 Harmonized dataset of ozone profiles from satellite limb and occultation measurements, *Earth Syst. Sci. Data*, 5, 349–363,
683 <https://doi.org/10.5194/essd-5-349-2013>, 2013.

684 Sofieva, V. F., Ialongo, I., Hakkarainen, J., Kyrölä, E., Tamminen, J., Laine, M., Hubert, D., Hauchecorne, A., Dalaudier, F.,
685 Bertaux, J.-L., Fussen, D., Blanot, L., Barrot, G., and Dehn, A.: Improved GOMOS/Envisat ozone retrievals in the upper
686 troposphere and the lower stratosphere, *Atmos. Meas. Tech.*, 10, 231–246, <https://doi.org/10.5194/amt-10-231-2017>, 2017a.

687 Sofieva, V. F., Kyrölä, E., Laine, M., Tamminen, J., Degenstein, D., Bourassa, A., Roth, C., Zawada, D., Weber, M., Rozanov,
688 A., Rahpoe, N., Stiller, G., Laeng, A., Clarmann, T. von, Walker, K. A., Sheese, P., Hubert, D., Roozendael, M. van, Zehner,
689 C., Damadeo, R., Zawodny, J., Kramarova, N., and Bhartia, P. K.: Merged SAGE II, Ozone_cci and OMPS ozone profile
690 dataset and evaluation of ozone trends in the stratosphere, *Atmos. Chem. Phys.*, 17, 12533–12552, [https://doi.org/10.5194/acp-](https://doi.org/10.5194/acp-17-12533-2017)
691 [17-12533-2017](https://doi.org/10.5194/acp-17-12533-2017), 2017b.

692 Sofieva, V. F., Szelag, M., Tamminen, J., Arosio, C., Rozanov, A., Weber, M., Degenstein, D., Bourassa, A., Zawada, D.,
693 Kiefer, M., Laeng, A., Walker, K. A., Sheese, P., Hubert, D., van Roozendael, M., Retscher, C., Damadeo, R., and Lumpe, J.
694 D.: Updated merged SAGE-CCI-OMPS+ dataset for the evaluation of ozone trends in the stratosphere, *Atmos. Meas. Tech.*,
695 16, 1881–1899, <https://doi.org/10.5194/amt-16-1881-2023>, 2023.

696 Solomon, S. C., Liu, H.-L., Marsh, D. R., McInerney, J. M., Qian, L., and Vitt, F. M.: Whole atmosphere climate change:
697 Dependence on solar activity, *J. Geophys. Res.-Space Phys.*, 124, 3799–3809, <https://doi.org/10.1029/2019JA026678>, 2019.

698 Szelag, M., Sofieva, V., Degenstein, D., Roth, C., Davis, S., and Froidevaux, L.: Seasonal stratospheric ozone trends over
699 2000–2018 derived from several merged data sets, *Atmos. Chem. Phys.*, 20, 7035–7047, [https://doi.org/10.5194/acp-20-7035-](https://doi.org/10.5194/acp-20-7035-2020)
700 [2020](https://doi.org/10.5194/acp-20-7035-2020), 2020.

701 Szeląg, M.E., Marsh, D.R., Verronen, P.T., Seppälä, A., and Kalakoski, N.: Ozone impact from solar energetic particles cools
702 the polar stratosphere. *Nat Commun* 13, 6883, <https://doi.org/10.1038/s41467-022-34666-y>, 2022.

703 Tamminen, J., Kyrölä, E., Sofieva, V. F., Laine, M., Bertaux, J.-L., Hauchecorne, A., Dalaudier, F., Fussen, D., Vanhellemont,
704 F., Fanton-d’Andon, O., Barrot, G., Mangin, A., Guirlet, M., Blanot, L., Fehr, T., Saavedra de Miguel, L., and Fraisse, R.:
705 GOMOS data characterisation and error estimation, *Atmos. Chem. Phys.*, 10, 9505–9519, [https://doi.org/10.5194/acp-10-](https://doi.org/10.5194/acp-10-9505-2010)
706 [9505-2010](https://doi.org/10.5194/acp-10-9505-2010), 2010.

707 von Clarmann, T., Glatthor, N., Grabowski, U., Höpfner, M., Kellmann, S., Kiefer, M., Linden, A., Mengistu Tsidu, G., Milz,
708 M., Steck, T., Stiller, G. P., Wang, D. Y., Fischer, H., Funke, B., Gil-López, S., and López-Puertas, M.: Retrieval of
709 temperature and tangent altitude pointing from limb emission spectra recorded from space by the Michelson Interferometer
710 for Passive Atmospheric Sounding (MIPAS), *J. Geophys. Res.-Atmos.*, 108, 4736, <https://doi.org/10.1029/2003JD003602>,
711 2003.

712 von Clarmann, T., Höpfner, M., Kellmann, S., Linden, A., Chauhan, S., Funke, B., Grabowski, U., Glatthor, N., Kiefer, M.,
713 Schieferdecker, T., Stiller, G. P., and Versick, S.: Retrieval of temperature, H₂O, O₃, HNO₃, CH₄, N₂O, ClONO₂ and ClO
714 from MIPAS reduced resolution nominal mode limb emission measurements, *Atmos. Meas. Tech.*, 2, 159–175,
715 <https://doi.org/10.5194/amt-2-159-2009>, 2009.

716 Waters, J. W., Froidevaux, L., Harwood, R., Jarnot, R., Pickett, H., Read, W., et al.: The Earth Observing System Microwave
717 Limb Sounder (EOS MLS) on the Aura satellite, *IEEE Trans. Geosci. Remote Sens.*, 44(5), 1075–1092,
718 <https://doi.org/10.1109/TGRS.2006.873771>, 2006.

- 719 Wilhelm, S., Stober, G., and Brown, P.: Climatologies and long-term changes in mesospheric wind and wave measurements
720 based on radar observations at high and mid latitudes, *Ann. Geophys.*, 37, 851–875, [https://doi.org/10.5194/angeo-37-851-](https://doi.org/10.5194/angeo-37-851-2019)
721 [2019](https://doi.org/10.5194/angeo-37-851-2019), 2019.
- 722 Yuan, T., Solomon, S. C., She, C.-Y., Krueger, D. A., and Liu, H.-L.: The long-term trends of nocturnal mesopause temperature
723 and altitude revealed by Na lidar observations between 1990 and 2018 at midlatitude, *J. Geophys. Res.-Atmos.*, 124, 5970–
724 5980, <https://doi.org/10.1029/2018JD029828>, 2019.